J Mater Sci

Polymers & biopolymers

Analysis of elastic and plastic behaviour in untreated pine wood under scratch test loads combining X-ray computed tomography and finite element simulations

Helena Ronkainen[1], Tero Harjupatana[2], Arttu Miettinen[2], Viacheslav Balobanov[1], Martti Venäläinen[3], Anni Harju[3], Veikko Möttönen[4], and Stefania Fortino[1,*]

[1] *VTT Technical Research Centre of Finland Ltd, P.O. Box 1000, 02044 Espoo, Finland*

[2] *Department of Physics, Nanoscience Center, and School of Resource Wisdom, University of Jyväskylä, Survontie 9, P.O. Box 35, 40014 Jyväskylä, Finland*

[3] *Production systems, Natural Resources Institute Finland, Vipusenkuja 5, 57200 Savonlinna, Finland*

[4] *Production systems, Natural Resources Institute Finland, Yliopistokatu 6B, 80100 Joensuu, Finland*

Received: 6 August 2025
Accepted: 29 December 2025

ABSTRACT

Wood is an anisotropic material, which affects its performance under different loading conditions. To understand the origin of surface failures occurring in wood under mechanical disintegration loads, an accurate investigation of its elastic and plastic behaviour is required. This study introduces a methodology that integrates experimental scratch testing, X-ray micro-computed tomography (μCT), and finite element simulations to examine the elastic and plastic deformation and failure behaviour of untreated pine wood under scratch loading. In the existing literature, scratch testing is primarily employed to assess coating adhesion or material abrasion resistance; its use for probing the mechanical response of wood remains limited. In the present study, scratches were applied to pine specimens in the radial, tangential, and longitudinal directions of wood using a diamond indenter under constant normal loads perpendicular to the scratched surface. The permanent residual depths measured by μCT were compared with FE-predicted deformations. The selected methodology enables quantification of the relationship between wood structure, loading conditions, and scratch performance. The results demonstrated that the regions with higher density favoured elastic deformation, whereas the residual scratch depth, reflecting plastic deformation, provided a reliable indicator of scratch resistance, exhibiting higher scratch resistance for the higher density wood. In particular, the wood with higher density showed residual depths in the range of 53–144 μm in radial direction scratches, whereas

Handling Editor: Gregory Rutledge.

Address correspondence to E-mail: stefania.fortino@vtt.fi

E-mail Addresses: helena.ronkainen@vtt.fi; tero.t.harjupatana@jyu.fi; arttu.i.miettinen@jyu.fi; viacheslav.balobanov@vtt.fi; martti.venalainen@wiksu.fi; tanni.harju@gmail.com; veikko.mottonen@luke.fi

https://doi.org/10.1007/s10853-025-12141-5

Published online: 13 January 2026

Springer

the less dense wood showed values between 90 and 300 µm. μCT imaging also revealed detailed deformation mechanisms and fracture pathways that develop under scratch-type loading. By coupling μCT with FE modelling for wood scratch mechanics, the work deepens the understanding of how wood microstructure responds to different scratch loading conditions. The findings can serve as a scientific reference for future experimental and numerical investigations of scratching, cutting and other disintegration loads in untreated wood and wood-based composites at the microscale.

GRAPHICAL ABSTRACT

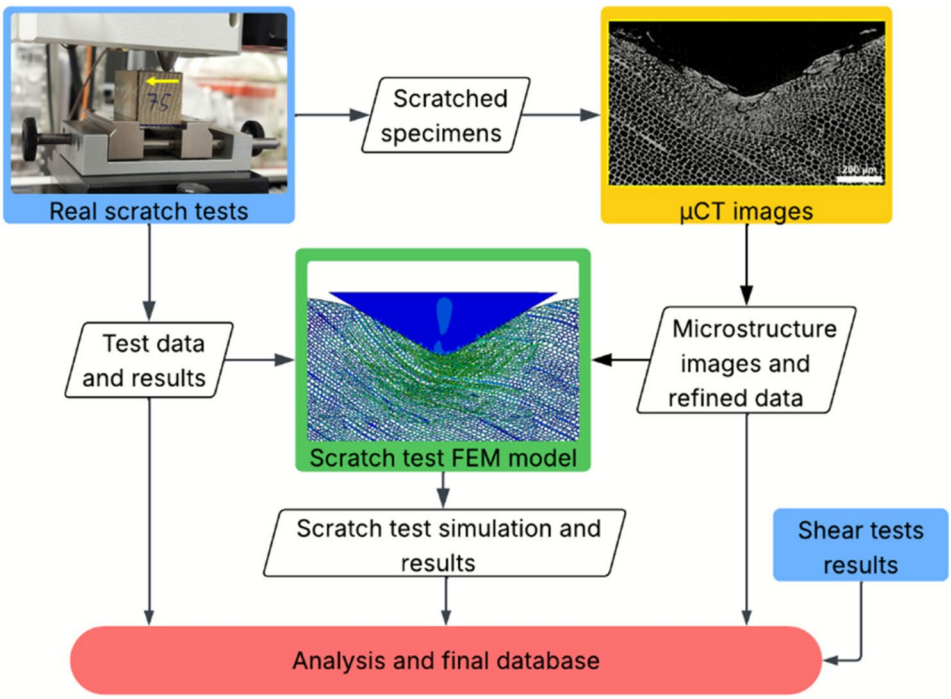

Introduction

Wood is a sustainable material that is commonly used as timber and in various wooden products due to its mechanical performance at both the material and structural levels [1]. It is also utilised in wood fibre materials and composites across several industrial sectors, such as construction, automotive, electronics and furniture.

Wood is characterised by a composite structure, consisting primarily of cellular and layered formations made up of three fundamental constituents: lignin, hemicellulose, and cellulose [2]. This intricate structure strongly influences the behaviour of wood, particularly its disintegration under different mechanical stresses. Therefore, a deeper understanding of the elastic and plastic behaviour of wood and its failure mechanisms under mechanical disintegration loads is important not only to optimise existing wooden products, but also for developing new wood-based composites. Considering the disintegration risks in wood products used in the construction and furniture industries, as well as in other industrial sectors, scratches are typical surface failures visible in structural materials. In addition to aesthetic problems, in some cases, large scratches can also generate crack failures and increase the number of cracks induced by moisture variations [3]. In this context, there is a need to evaluate the scratch resistance of wood in a quantitative manner. As argued in [4], disintegration phenomena at the nano- and microscale are relevant in many applications, such as pulp production, wood cutting, nano- or microfibril cellulose manufacturing, and particleboard defibration. To address questions

related to the deformation and scratch performance of wood materials, scratch testing can be used as a tool for evaluation.

In the scratch test method, an indenter is loaded against the sample surface, while the sample moves with a constant velocity. The scratch test has previously been widely used to study adhesion of the coatings ([5–7]) and to investigate crack initiation for determining the fracture toughness of coatings [8]. Also, the scratch resistance of composite materials has been investigated in relation to fibre orientations [9]. A study examining the scratch resistance of furniture lacquer coatings by scratch test demonstrated good repeatability of the results on the same piece of furniture and good reproducibility across different pieces of furniture [10].

However, in the existing literature, the use of scratch tests for wood materials is still limited. The combination of indentation, scratch, and wear tests was used by Hermann et al. [11] to study the performance of UV-cured coatings of wood products under different loads. Hardness, abrasion, scratch, and wear resistance were studied in relation to various coating formulations based on different monomer–oligomer couples. The scratch experiments showed that hard and brittle coatings failed at lower loads compared to the soft and ductile ones. Before failure occurred, plastic deformation took place due to indenter penetration into the surface. Scratch tests have also been combined with nanoindentation tests to obtain radial profiles of the mechanical properties (e.g. micro- and meso-hardness and elastic modulus) of cross-cut Scots pine samples in [12]. The used technology allowed accurate determination of the width of annual growth rings for evaluating the quality of wood for use in dendrochronological applications.

Previously, some of the authors have studied the scratch performance of green wood with polyethylene glycol (PEG) impregnation simulating different moisture contents [4]. The results allowed analysis of the penetration depth of the tip, which described the deformation of swollen wood, and demonstrated that the scratch performance of wood samples was dependent on PEG concentration, density, indenter tip size and tip material, normal force and scratching direction.

During scratch testing, tensile, compressive and shear stresses are present under the indenter [8]. In the complex anisotropic wood material, the high and concentrated stresses and strains can generate permanent deformations or failures. The plastic deformation of uncoated and untreated wood under scratch-type loading has not been studied in depth in the current literature. Therefore, the present paper proposes combining scratch testing with X-ray microtomography (μCT), a non-destructive imaging method that quantifies morphology of scratches in 3D with spatial resolution down to 1 μm or even below. This combination aims to measure accurately the plastic deformation generated by scratch-type loads. Additionally, μCT also provides insight into the deformation and failure mechanisms occurring in the wood structure under scratching loads. Finite element modelling (FEM) is also applied to increase understanding of the stresses and strains occurring in the wood structure under scratch-type loading.

The μCT has been used to study the microstructure of wood materials and coatings, but there are only a few studies that have utilised its potential to investigate indentation and scratch resistance, and the related deformation and fracture mechanisms. A study on the scratch resistance of a hard-on-soft polymer bilayer [13] showed that the hard coating reduced the plastic deformation of the substrate at low loads. However, with increasing loads, the hard coating showed three different fracture mechanisms that were studied using μCT. The mechanical behaviour of wood has also been studied by incrementally indenting a needle into the wood surface and measuring the resulting strain fields from μCT images [14]. The results showed larger strains, and a deeper crack initiation zone compared with the predictions based on the classical continuum theory. Given the limited literature, combining μCT with scratch testing can provide new insights into deformation mechanisms in untreated wood at the microstructural level.

In the literature, numerical modelling, particularly finite element modelling, of wood and wood-based materials is widely presented. Florisson and Gamstedt [15] presented a thorough review of μCT-aided finite element modelling of wood. Numerous studies have focused on the macro-scale, such as microstructure-informed macro-model [16] or on fibre-level (meso-scale) simulations [17], where special type of polygonal finite elements was used to represent the cellular microstructure of wood. Also, a well-developed macro-scale model that incorporated fibre orientation and natural inhomogeneities has been presented [18]. Micro-scale models of the wood microstructure are not uncommon in the literature as well ([19–22]);

however, the application of such models to investigate highly localised mechanical deformation and related effects, such as those observed in micro-scratches, remains relatively scarce.

The research gap covered in the present work is the need to evaluate the deformation performance and permanent deformation of wood under scratch loading to assess scratch resistance. The scratch tests were carried out on wood samples, and μCT was used to measure the residual depth of the scratch grooves. Combining this measure with the penetration depth obtained during scratch testing, the magnitude of the elastic and plastic deformation could be determined. Furthermore, high-resolution μCT imaging enabled analysis of deformation and failure mechanisms associated with scratching. Image-based FEM models were also generated based on μCT images to simulate the scratch tests and complement the information provided by μCT with the study of local strains and stresses generated by scratch loads.

Materials and methods

Preparation of untreated pine samples

A Scots pine tree from a naturally regenerated stand in Mäkrä, Kerimäki, Finland (N 61°50′, E 29°23′) was harvested on 29th November 2022 for this study. The stand belongs to the network of EVOLTREE intensive study sites, ISS (http://www.evoltree.eu/index.php/intensive-study-sites/map). The tree was selected based on earlier studies initiated in 2011 (unpublished data) and 2018 [23], which focused on stilbene and resin acid content in the outer heartwood and on heartwood radius. A representative average tree was selected from several candidates. The pine's cross-measured diameter at a height of 1.3 m was 290 × 272 mm (excluding bark), with 54 growth rings. The heartwood diameter was 150 × 140 mm, comprising 21 growth rings. The butt log up to a height of 3 m was cut into blocks of approximately 30 cm in length and stored at − 20 °C until further processing.

Test specimens for shear strength measurements were prepared from a 5-cm-thick disc sawn from a block stored at − 20 °C. The discs were conditioned in a constant-climate chamber (relative humidity RH: 65%, temperature T: 20 °C) until their mass stabilised. The final dimensions of the shear test specimens were 20 mm × 40 mm × 40 mm, representing the locations of the specimens of the scratch test such that the area of one shear test specimen corresponded to a combination of two scratch test specimens with an area of 20 mm × 40 mm. The shear test specimens were prepared separately from heartwood and sapwood.

For the scratch tests, samples were cut from a thick disc sawn from the same Scots pine tree. The disc was cut into samples measuring 20 mm × 20 mm × 30 mm samples as shown in Fig. 1. The samples numbered from 44 to 69 were selected for scratch tests, as they provided a representative coverage of different regions of the tree cross section. After cutting, the samples were stored in a controlled laboratory environment (50 ± 5% RH, 21 ± 1 °C) prior to and during the tests, and therefore, the samples were subjected to natural drying before the scratch tests. After the scratch tests were carried out on all the designated samples, the moisture content and density of the samples were determined. The moisture content ranged from 11.5 to 12.9%. The wet densities varied between 399 and 556 kg/m^3 (Table 1), with sapwood exhibiting a higher average density (509 kg/m^3) compared to heartwood (454 kg/m^3). The scratch tests were carried out on all twenty-five samples. Samples 64 and 65 from the central region of the wood cross section, representing the heartwood, and samples 63 and 69 from the outer rim of the wood cross section, representing the

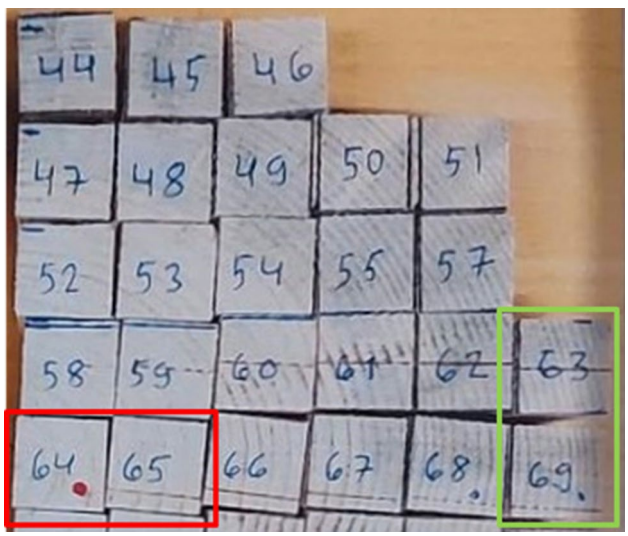

Figure 1 Wood samples cut from the cross-sectional disc of the Scots pine tree selected for scratch tests were numbered from 44 to 69. The selected samples represent one quarter of the entire disc. Samples 64 and 65, representing heartwood outlined in red, and samples 63 and 69, representing sapwood outlined in green, were used for μCT imaging.

Table 1 Wet density (Ru) and dry density (Ro) of the samples determined after scratch testing

Sample number	44	45	46	47	48	49	50	51	52	53	54	55	57	58	59	60	61	62	63	64	65	66	67	68	69
Wet density *Ru* (kg/m^3)	499	529	538	470	469	530	484	493	445	454	469	462	516	399	422	484	501	506	548	420	419	484	496	519	556
Dry density *Ro* (kg/m^3)	444	472	478	419	417	442	431	438	398	406	418	411	458	358	379	434	444	450	487	376	376	434	441	462	494

sapwood, were selected for the μCT analysis described in Sect. "X-ray microtomography". In addition, two samples (8 and 23), representing sapwood and heartwood, respectively, were also scratched and used to evaluate the accuracy of the μCT-based scratch depth analysis.

Scratch tests

The scratch tests were carried out with a Micro-Combi Tester (CSM Instruments, Antor Paar). In the scratch test, a diamond indenter (Rockwell C) was loaded against the surface while the sample was moved in a controlled manner, causing compressive, shear and tensile stresses under and around the indenter and generating a scratch groove on the sample surface [8]. The diamond tip with a radius of curvature of 200 µm, fixed in a conical steel indenter (120° apex angle), was used for the scratch tests. A constant normal load was applied using three load levels, namely 4, 10, and 20 N. The scratch length was 10 mm, and the scratching speed used was 10 mm/min. The scratch tests were carried out on three sides of each wood sample, representing the different directions of the wood structure. Figure 2 illustrates the three scratch directions, with the R direction going across the growth rings, the T representing the tangential direction, and the L being the longitudinal (vertical) direction of the wood structure. One scratch was made for each direction and load case on the wood samples. The scratch tests were carried out in a controlled environment of 50 ± 5% RH and temperature 21 ± 1 °C.

During scratch testing, the normal force F_n, friction force F_μ (the force resisting the scratch movement), penetration depth Pd (the sum of elastic and plastic deformation during scratch test), and acoustic emission AE were measured. The friction coefficient μ was determined by dividing the friction force by the normal force. The residual depth (Rd) values of the scratches (the remaining plastic deformation of the material) were determined from μCT images of the scratch grooves as described below.

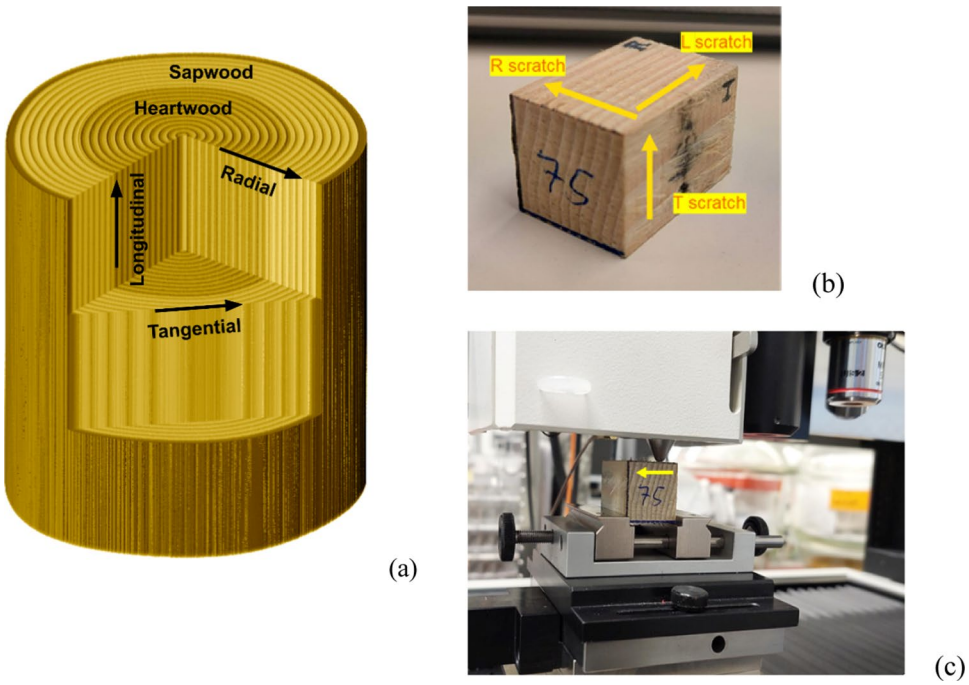

Figure 2 **a** Schematic crosscut of a tree illustrating the scratch directions R (radial), T (tangential), and L (longitudinal) in scratch testing; **b** Scratch directions R, T, and L in the wood sample; **c** The test sample positioned in the sample holder of the Micro-Combi tester used for scratch testing.

Shear strength measurements

The shear strength tests were conducted to study the mechanical performance of heartwood and sapwood under shear loading, and to assess whether shear strength correlates with scratch performance. The shear strength measurements were performed using a universal materials testing machine Zwick Z050 (ZwickRoell, Germany) according to ISO 13061-8:2022. Before the shear test, the dimensions of the specimens were measured with a calliper at an accuracy of 0.1 mm in the radial and tangential directions to calculate the shear area. The loading was done in the longitudinal direction at a steady speed of 2 mm/min, causing the test specimens to break within 1–2 min. The shear strength of a specimen was calculated by dividing the maximum load by the shear area.

X-ray microtomography

X-ray microtomography (μCT) was performed on selected samples after the scratch tests with different loads and directions. Medium-resolution imaging was used to measure scratch morphology, whereas high-resolution imaging focused on deformation mechanisms within the wood cell structures. Because μCT resolution depends on sample size, scratched samples were cut into smaller subsamples to achieve higher resolution. Two additional samples (8 and 23) were imaged in their entirety (20 mm × 20 mm × 30 mm) both before and after scratching for method validation (see Sect. "Determination of scratch dimensions"). The principles of sample preparation for medium- and high-resolution imaging are shown in Fig. 3.

For medium-resolution imaging, scratched areas of samples 63, 64, 65, and 69 were cut into subsamples (12 mm × 12 mm × 5 mm) containing all three scratches generated under different normal loads (4, 10 and 20 N) in one of the directions (R, T or L). For high-resolution imaging, subsamples from 64 and 69 were further cut into smaller pieces (2 mm × 2 mm × 10 mm), each containing approximately 2 mm-long scratch segments. To stabilise these fragile subsamples and maximise the visible scratch length, each piece was glued at both ends to a semi-cylindrical carbon fibre rod. The rods were then ground to a round shape (1.8 mm diameter) using a custom-made grinding device, to ensure proper fit within the reconstruction field of view (2.2 mm in diameter).

Determination of scratch dimensions

The twelve subsamples from samples 63, 64, 65, and 69 (Fig. 3c) were imaged using an in-house-built JTomo microtomograph (University of Jyväskylä) with a

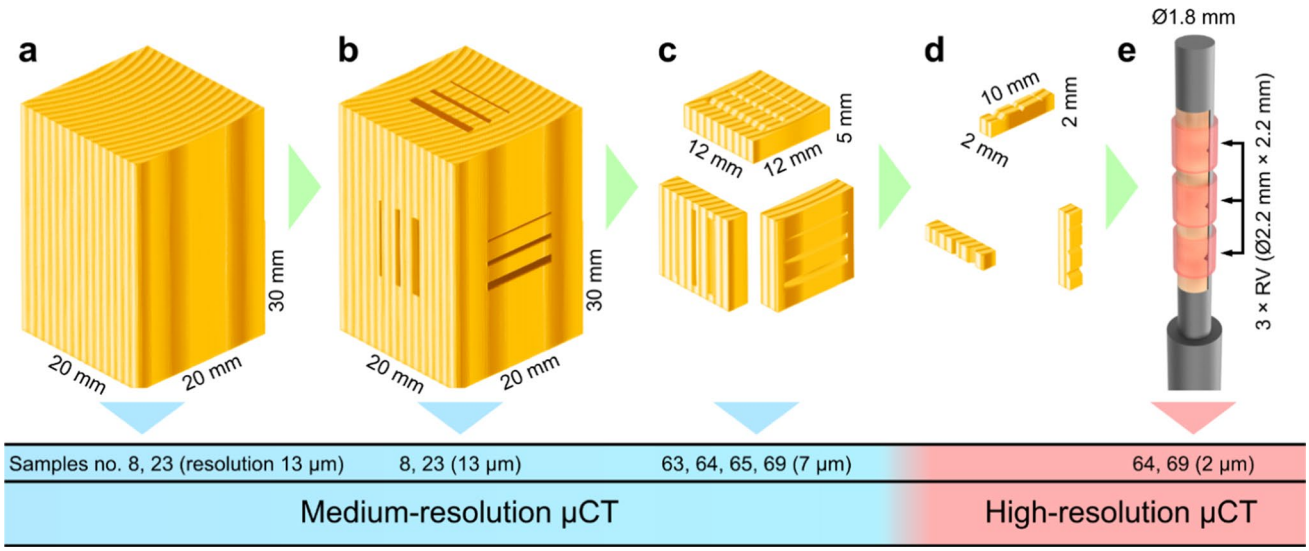

Figure 3 Sample preparation for X-ray microtomography. Two samples were imaged **a** before and **b** after the scratch tests in their entirety. **c** Four samples were imaged only after the scratch tests by extracting subsamples containing the scratches. **d** Two subsamples were further cut into smaller pieces, attached to carbon fibre rods, and trimmed to a smaller size to fit into the reconstruction volume (RV) for high-resolution μCT.

voxel size of 7.0 µm. The X-ray tube (Hamamatsu L12161-07) was operated at 40 kV and 200 µA (small focus mode), without a filter. A flat-panel detector (Teledyne Dalsa Shad-o-Box 6K HS) recorded a total of 3000 projection images of size 2940 × 2304 pixels, each with an exposure time of 2 s, during a continuous rotation of 360°. This resulted in a total scan time of approximately 2 h for each subsample, including beam stabilisation and the acquisition of reference images. Reconstructions were performed using the filtered back-projection algorithm, implemented in the in-house-developed pi2 software [24].

The reconstructed volume images (Fig. 4a and b) were converted to binary images (air = 0 and wood material = 1) slice by slice using 2D median filtering (radius = 10 pixels) followed by manual thresholding (Fig. 4c). For each cross-sectional slice, the surface profile was calculated by summing the pixel values in each column. As the surface profiles were slightly curved in most cases, they were straightened by fitting quadratic polynomials to the profiles, excluding data at the scratch locations. This fit also defined the baseline level for determining scratch depth, since the original surface level at the scratch locations was not known. To obtain the dimensions of the scratches, a sum of Gaussian functions $y = \sum_{i=1}^{3} d_i \cdot \exp\left[-\left(x - x_{c,i}\right)^2 / \left(2\sigma_i^2\right)\right]$ was fitted to each straightened profile (Fig. 4d). The amplitude d_i directly represented the depth of scratch i. Repeating the process for each cross-sectional slice then gave the scratch depth as a function of position along the scratch. Residual depths of the scratches generated in samples 63, 64, 65, and 69 were used for analysis of the scratch test results.

To verify the reliability of the depth profile measurement method based on post-scratch images, two additional samples, 8 and 23, were included for validation. These samples were imaged both before and after scratch tests using JTomo with the same settings as above, but now at a resolution of 12.7 µm (Fig. 3a and b) to ensure that the entire sample fitted within the reconstruction volume. The μCT images taken before and after scratch tests were registered and binarised, and a difference image was calculated, leaving only the scratches visible (pixel values 1 for the scratch groove and 0 elsewhere). For each cross-sectional slice perpendicular to the scratches, scratch depth was calculated by summing the pixel values in each column and taking the maximum value of the resulting set. This two-image method was considered more accurate and suitable for validation, since it directly measured the distance from the bottom of the scratch to the known surface of the pre-imaged sample. However, it was more complex and labour-intensive, since aligning the images in three dimensions with respect to translations and rotations was challenging and required both visual inspection and digital volume correlation techniques. Furthermore, the samples had slightly shrunk between the images, so scaling was needed in each dimension, and even after this, each scratch area had to be aligned separately.

Comparison of the two methods showed reasonable agreement between residual depth profiles

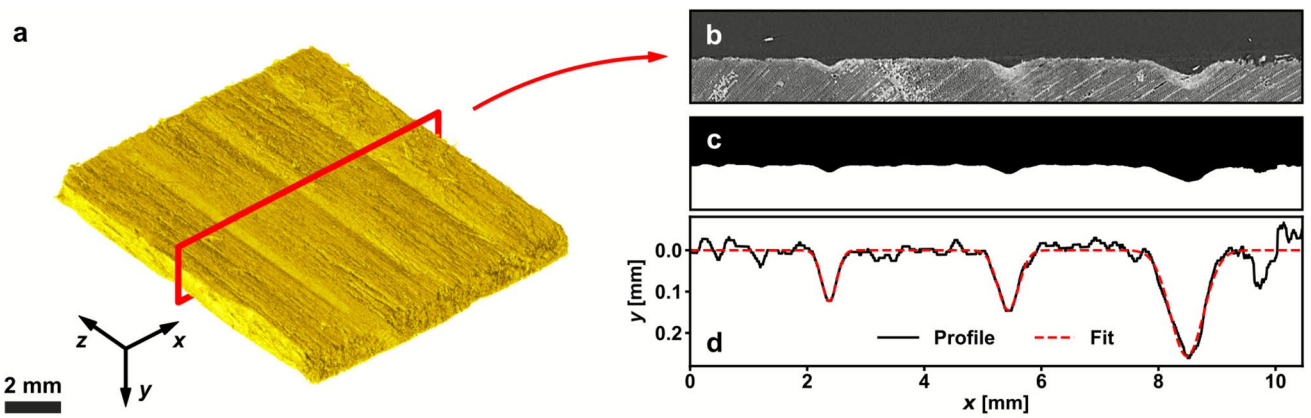

Figure 4 Measurement of the residual scratch depth profiles based on **a** μCT images analysed **b** slice by slice along the scratches. **c** Each slice was converted into a binary image, **d** which was used to calculate the surface profile. The depth and width of each scratch were determined by fitting a sum of Gaussian functions to the profile.

(Appendix 1, Figs. 17, 18 and 19), confirming that depths determined from post-scratch images alone were sufficiently reliable for the purposes of this study and allowing the scratch depth measurements to be performed more efficiently using only post-scratch images. However, irregular and splintered scratches, particularly in some regions of certain scratches, remained challenging for accurate depth determination with both methods.

High-resolution μCT images to investigate deformation mechanisms

The voxel size of 7–13 μm, used in the medium-resolution μCT scans, was insufficient to resolve the individual cell structure of the wood required for analysis of the deformation mechanisms of wood cells. Therefore, high-resolution μCT imaging was performed for the twelve subsamples from samples 64 and 69 that contained segments of each of the three scratches representing different normal loads and scratch directions (Figs. 3d and e). The scratches were imaged using an Xradia MicroXCT-400 microtomograph with a voxel size of 2.2 μm (10 X objective). The X-ray tube was operated at 40 kV and 100 μA without a filter. A total of 753 projection images with a size of 1000 × 1000 pixels (binning 2) were acquired with an exposure time of 2 s over a stepwise rotation of 188°. As only one scratch fitted in the field of view (2.2 mm × 2.2 mm) at a time, each sample was scanned three times, resulting in a total scan time of approximately 7 h. All twelve scans were reconstructed into high-resolution volume images using the same pi2 software as employed for medium-resolution imaging.

Finite element modelling of wood structure

To simulate the scratching experiment, a two-dimensional finite element (FE) model was developed using high-resolution μCT images processed in the software OOF2 [25]. The model was based on the μCT image of heartwood sample number 64 (Fig. 5a). It represents the specimen's cross section perpendicular to the trajectory of the scratching indenter. Due to the conical, axisymmetric shape of the indenter's tip, its motion through a single fixed cross section during scratching can be modelled in 2D as an indentation process. This formulation is considered to be a good approximation of the processes occurring within a single cross section during the physical scratching experiment, offering a simplified yet insightful perspective on the deformation process in wood on the microstructural level.

To obtain a 2D analogue of the force applied with a 3D indenter in the physical experiment, a series of auxiliary problems was solved (Fig. 5b). A piece of bulk material, with material properties equivalent to those used for wooden cells, was indented in a 3D formulation by a rigid indenter under applied forces F_{3D} of 4, 10, and 20 N. For each of these load cases, the corresponding maximum penetration depths were calculated. Then, analogous problems were solved in 2D to achieve the same penetration depths and to determine the reaction forces. The values of these reaction forces are considered as the equivalent 2D loadings, F_{2D}, and were found to be 18.5, 31.3, and 62.0 N, respectively.

The image-based FE model from Fig. 5a was replicated six times, and these segments were seamlessly connected by manual merging of the finite elements, as presented in Fig. 5d. The interfaces between these segments are indicated by black dashed lines. Symmetric boundary conditions (restriction of normal displacements) were applied on the edges highlighted in blue, constraining displacements normal to those edges. The applied loads, although depicted as a concentrated force, were in fact distributed along the line (surface in 3D) representing the outer edge of the indenter tip. The type of elements corresponds to the plane strain formulation. Abaqus/Explicit was used as the FEM solver [26].

A simple elastoplastic material model was employed for wooden cells (Fig. 5c), with the Young's modulus of $E = 5.3$GPa and Poisson ratio $\nu = 0.3$. The yield stress was defined as $\sigma_{Y02} = 80MPa$, and plastic behaviour was modelled as linear hardening with a plastic modulus $H = 2$GPa. The rigid indenter was modelled using the elastic properties of diamond ($E = 1050$GPa, $\nu = 0.2$). The chosen values for material parameters were in the range of those reported in the literature ([12], [27], [20]. The material values of wood depend drastically on factors such as age, humidity, and temperature. The values determined via nanoindentation measurements are very dependent on the location of the indents and on the structural layers, and the macro-scale measurements of wood provide values for Young's modulus from some units of GPa to some tens of GPa, and yield in the range of 50–100 MPa, which introduces uncertainty into the modelling approach. Additionally, the 2D formulation itself tends to make the material stiffer than in reality,

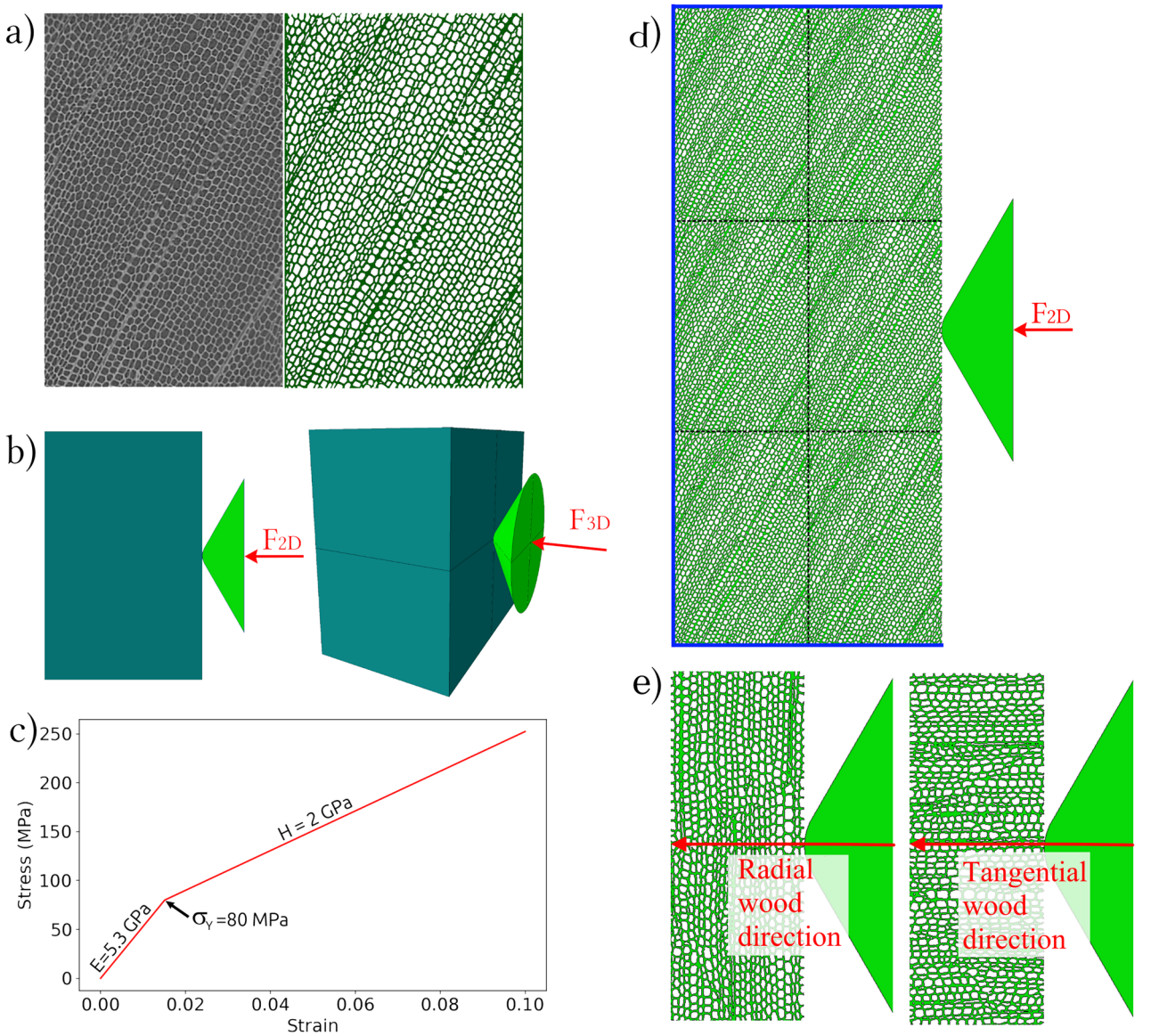

Figure 5 2D Finite element model of the wood cell structure representing heartwood sample 64. **a** μCT image and the corresponding finite element model. **b** Auxiliary problem formulation used to translate experimental 3D loading into the 2D model. **c** Tensile curve of the wooden cell material used in the FEM simulations. **d** 2D FEM problem formulation of the scratching process; blue lines indicate symmetric boundary conditions. **e** Two additional problem configurations with indentation loading applied parallel to the radial wood direction and parallel to the tangential wood direction.

which may dictate the use of slightly lower values of Young's modulus to achieve realistic results.

To demonstrate the applicability of the model, two supplementary problems were solved. In these cases, the solution domain was rotated and accordingly trimmed to obtain rectangular shapes that were constrained by the same symmetric boundary conditions considered above. The domain was oriented such that the indenter loaded the wood structure in the radial wood direction in one case and in the tangential wood direction in the other case, see Fig. 5e. This approach allowed for the investigation of the model's response under loading conditions aligned with the material wood directions. The 2D loading equivalent of $F_{3D} = 4N$ was applied to the indenter in both cases.

Results

Shear strength

Shear strength on the Scots pine heartwood and sapwood samples is presented in Table 2. The results were comparable to shear strength values for wood in different regions of Finland and Sweden reported by Grekin and Surini [28]. They obtained average shear strength values of 7.7–8.3 MPa and 8.3–9.5 MPa in Scots pine heartwood and sapwood, respectively. In comparison, it should be taken into account that in this study, the data were collected from only one tree, unlike the study carried out in [28], where the total number of trees was 180.

Scratch tests

The friction force evolution differed between scratch directions, as presented in Fig. 6. Scratching in the radial direction resulted in the highest variation in friction force, as the indenter was moving across the growth rings of the wood. This phenomenon is very distinct for the sapwood sample 69, which shows the fluctuation of the friction force increasing with increasing normal load applied. The heartwood sample 65 had similar performance, but with a lower rate of fluctuation. Comparison of those two samples also showed the difference in the distance between the growth rings, reflecting the density difference between the samples. For scratches performed in the tangential direction, the structural features of the wood were less pronounced, and the fluctuation of the friction force was reduced for all normal loads. In the longitudinal direction, the variation was further reduced, resulting in relatively smooth friction force curves during testing.

The penetration depth measured during the scratch testing had similar trends compared to the friction force values, as can be observed in Fig. 7, where the penetration depth evolution during scratching of samples 65 and 69 in the radial direction is presented. The wood structure in radial direction consists of growth rings with alternating hardness, which influences both penetration depth and friction force performance. Typically, the penetration depth increased as the indenter moved across the softer regions of the wood structure, and the friction force decreased simultaneously. Conversely, the penetration depth decreased, and the friction force increased when the indenter passed over harder regions.

To enable comparison between different samples, the measured friction force and penetration depth values were averaged along the scratch length. The average values, together with their standard deviations for all measured samples, are presented in Appendix 1 (Tables 4 and 5). Due to fluctuations associated with the structural features of the wood, the scatter of the average values ranged from 11 to 44% in the radial direction, from 8 to 32% in the tangential direction, and from 3 to 20% in the longitudinal direction.

When the averaged friction force values were plotted as a function of wet density (Ru) for all 25 samples, a slightly decreasing trend friction force was observed as the density was increased. The trend was most pronounced for the tests with normal loads of 4 and 10 N, yet the scatter remained relatively high, as can be observed for the tests with 4 N normal load in Fig. 8**.** Although a decreasing trend can be identified, the coefficient of determination (R-squared) of the linear equation was low. The increase in density appears to restrict the penetration of the scratch tip into the wood structure, thereby reducing the ploughing friction. For the tests with the highest normal load of 20 N, no clear trend was observed, as the high normal load seemed to override the effect of density.

The average friction force values measured for the heartwood samples (64 and 65) and the sapwood samples (63 and 69) in scratch tests performed with normal loads of 4, 10, and 20 N in the R, T, and L directions are presented in Fig. 9. The penetration depth Pd (Fig. 9a), measured during the scratch testing, represents both elastic and plastic deformation of the wood under the applied load. The residual depth Rd of the scratch grooves was determined by μCT after the scratch tests as described in Sect. "Determination of scratch dimensions". The residual depth (Fig. 9b) represents the remaining plastic deformation of the wood structure. The elastic deformation Ed (Fig. 9c) was determined by

Table 2 Shear strength of wood measured parallel to the grains (longitudinal wood direction) for sapwood and heartwood samples

	Number of specimens	Shear strength (MPa)	Min	Max	SD
Sapwood	23	10.00	7.20	12.36	1.19
Heartwood	12	7.95	5.03	9.99	1.44

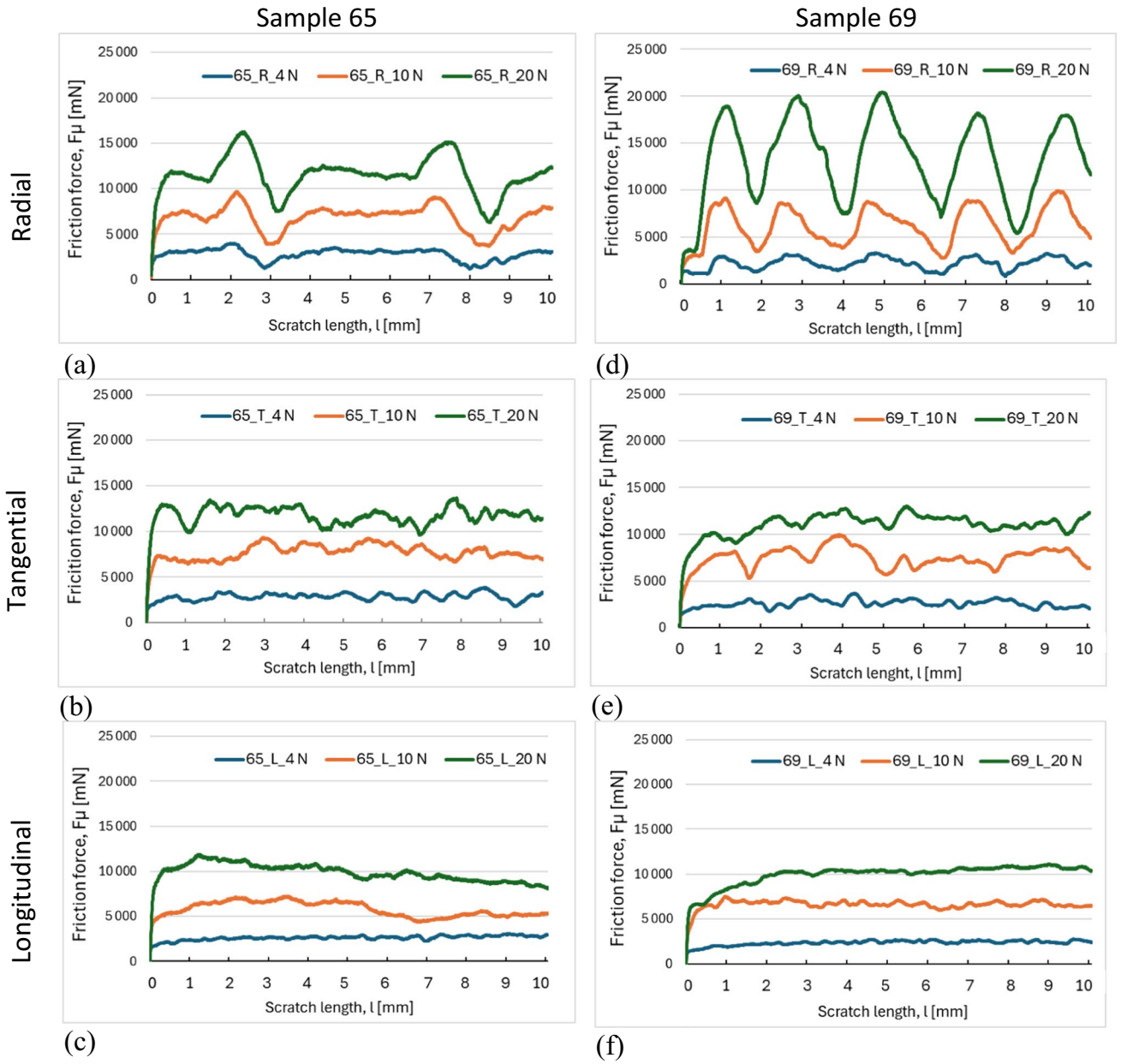

Figure 6 The friction force (Fμ) evolution during scratch testing of sample 65 (heartwood) in **a** R, **b** T, and **c** L directions, and of sample 69 (sapwood) in **d** R, **e** in T, and **f** in L directions. The normal loads applied during testing were 4 N (blue line), 10 N (orange line), and 20 N (green line).

subtracting the residual depth of the scratch grooves from the penetration depth measured during testing. Figure 9 shows that increasing the normal load generally increased the penetration depth and the friction force in a predominantly linear manner.

With respect to the penetration depth, the heartwood experienced higher friction forces compared to sapwood in all scratch directions and at all normal loads applied. This was most evident in the R direction, where the penetration depth was clearly higher than that of sapwood as shown in Fig. 9a. Similar trends were also observed for the T and L directions.

When comparing the plastic deformation performance (Fig. 9b), the less dense heartwood samples exhibited greater residual depths and thus a greater share of plastic deformation in all directions. At the

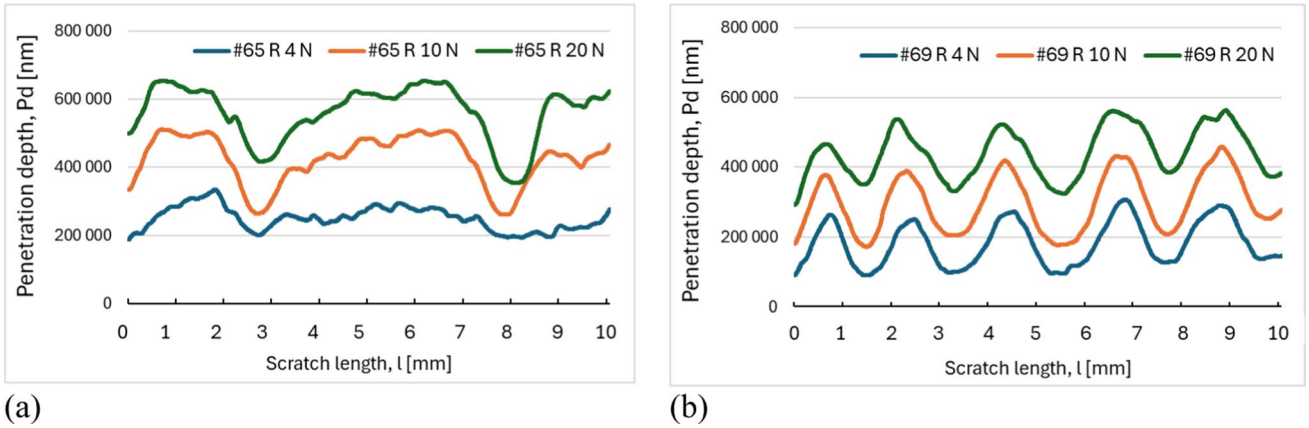

Figure 7 The penetration depth (Pd) evolution during scratch testing in the R direction of **a** sample 65 (heartwood), and of **b** sample 69 (sapwood). The normal loads applied during testing were 4 N (blue line), 10 N (orange line), and 20 N (green line).

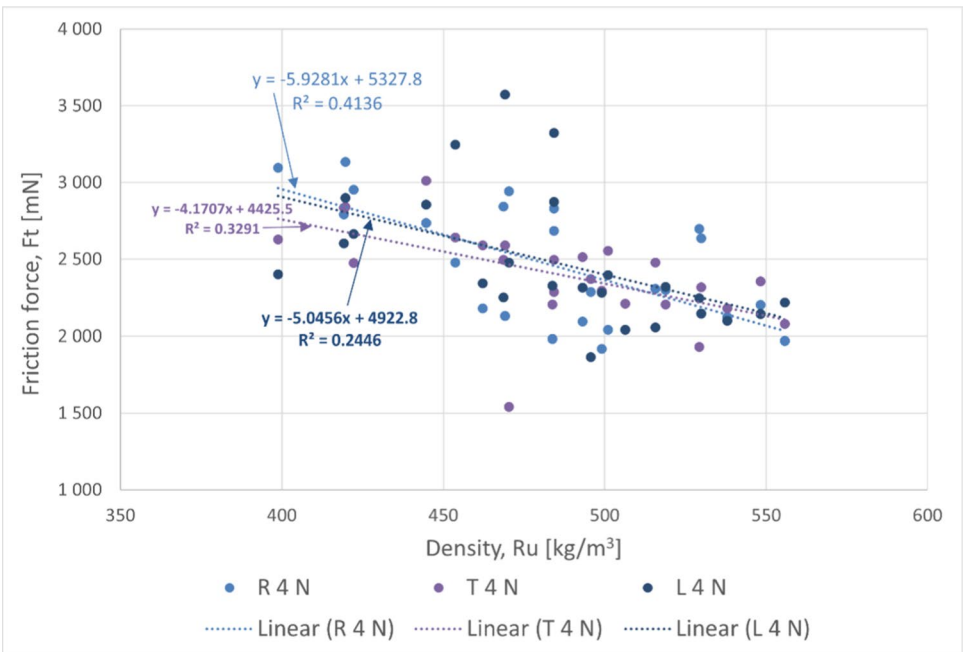

Figure 8 The friction force as a function of wet density of 25 samples in scratch tests carried out in the R, T, and L directions with the normal load of 4 N. The linear trendlines are presented with the equations and the R^2 values.

same time, the higher density sapwood had higher elastic deformation, indicating higher elasticity and improved recovery of the wood structure (Fig. 9c).

The elastic deformation of wood represents the capability of this material to recover after the load is released. Since the elastic and plastic deformation differ, the ratio of elastic deformation to plastic deformation for heartwood samples (64 and 65) and sapwood samples (63 and 69) was determined for different loads and scratch directions. The sapwood samples had higher density compared to the heartwood, and they also had more pronounced elastic deformation as observed in Fig. 10. This is evident particularly for the R and T directions, whereas in the L direction, the ratios are at a similar level.

Results of X-ray microtomography

The residual depth and scratch width values of the scratches were determined via the medium-resolution μCT post-scratch images of samples 63, 64, 65, and 69. The determined residual depths of the scratches as a function of position along the scratches were also compared to the penetration depth. The results

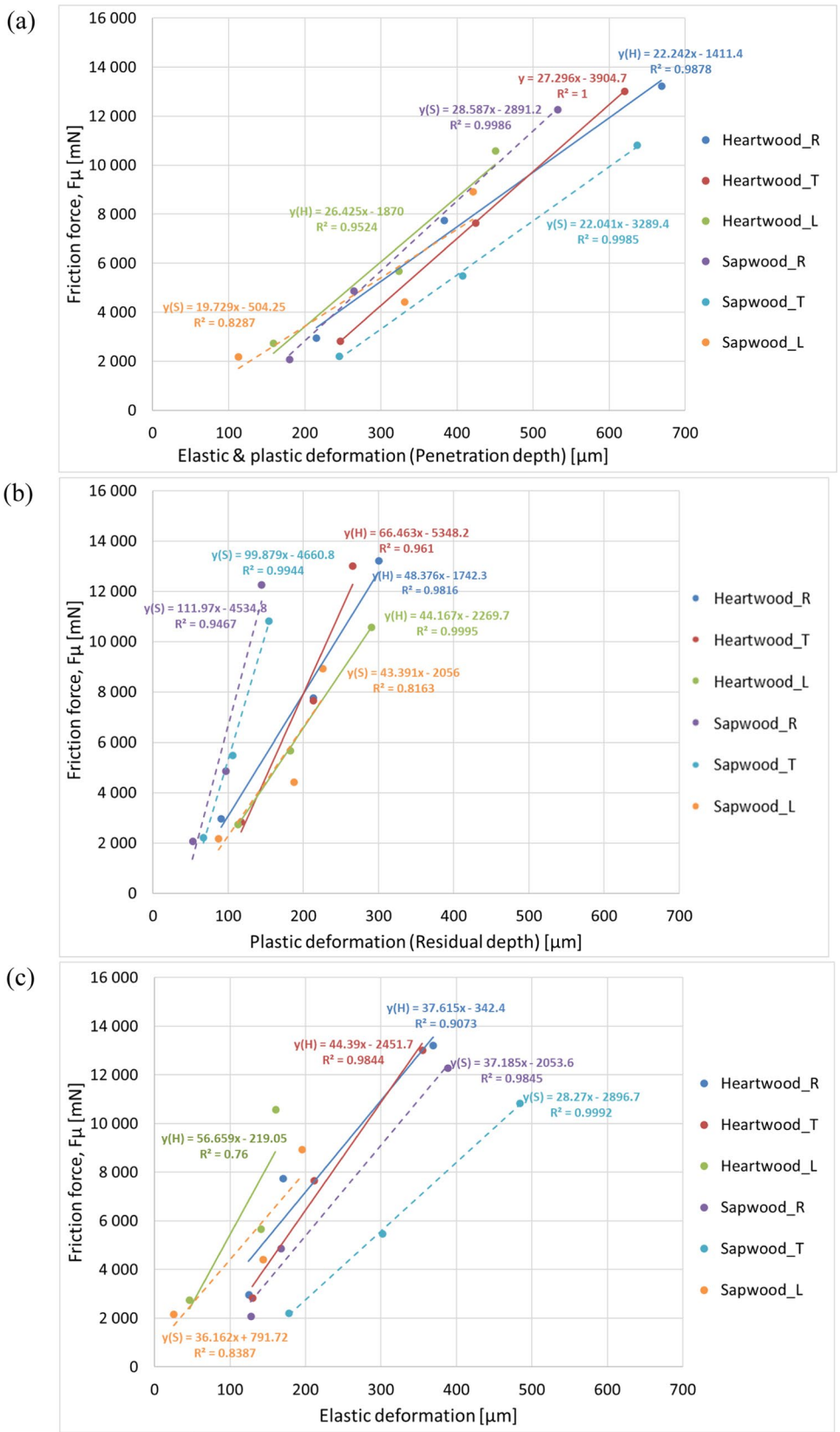

Figure 9 Friction force during scratch testing for heartwood samples (64 and 65) and sapwood samples (63 and 69) for normal loads (4, 10 and 20 N) and in the different scratch directions R, T, and L as a function of the **a** elastic and plastic deformation (penetration depth Pd), **b** plastic deformation (residual depth Rd), and **c** elastic deformation (Ed). The linear trendlines are presented with the equations and the R^2 values. The trendlines for heartwood samples are presented with solid lines, and the trendlines for sapwood samples are presented with dashed lines.

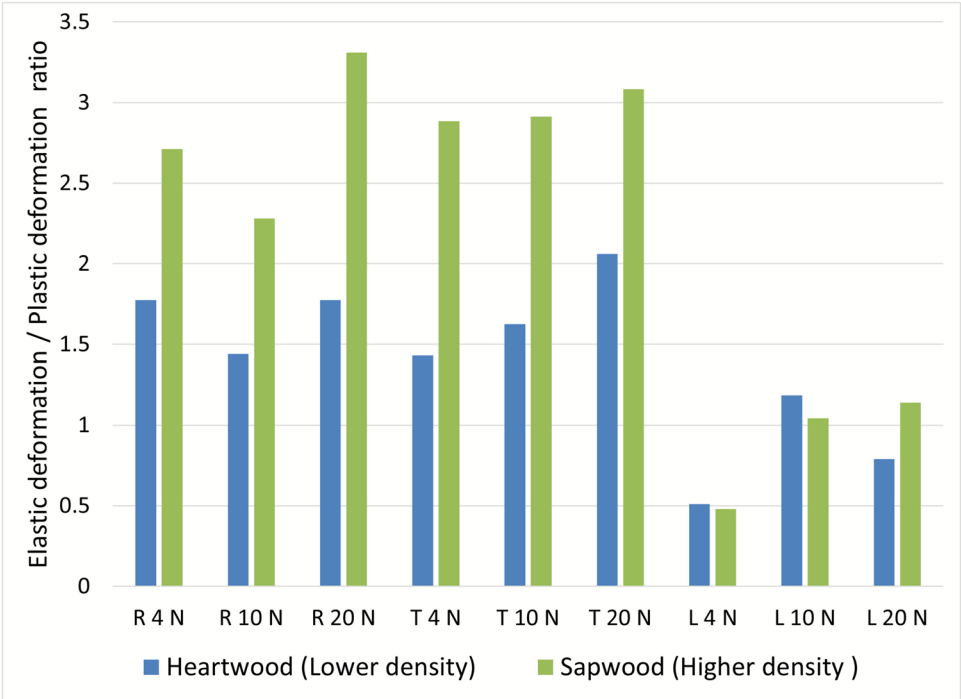

Figure 10 The ratio of elastic deformation to plastic deformation for heartwood and sapwood with different normal loads and scratch directions.

are presented as graphs in the additional information Appendix 2 (Figs. 17, 18 and 19). The values averaged over the scratch length for all samples are presented in the additional information in Appendix 3 (Table 6).

The residual depth values of the scratch grooves of the samples 63 and 69, representing sapwood, and of the samples 64 and 65, representing heartwood, measured with μCT, are presented as average values of the samples in Fig. 11. The graph shows that in most cases, the heartwood had a larger residual depth compared to the sapwood. Only for the L direction, the difference was not consistent in all cases. For some samples, the deviation of results was rather high, which is related to the structural differences between otherwise similar samples.

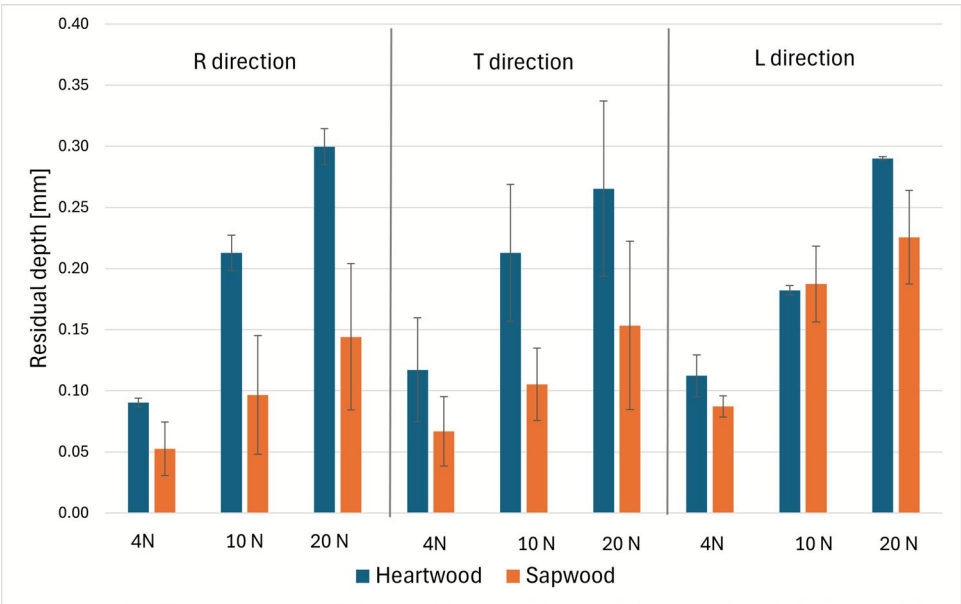

Figure 11 The residual depth of the heartwood samples (64 and 65) and the sapwood samples (63 and 69) measured with μCT on the scratches generated in the R, L, and T directions with the normal loads of 4, 10, and 20 N

Figure 12 presents high-resolution μCT images of heartwood sample 64 (lower density), scratched in the longitudinal (L) direction. The images show the densification of the cell structure of the wood with increasing width of the densified layer on the surface as the scratch load was increased. This can be verified by the solid fraction graphs accompanying the images. The densification occurs only near the surface of the scratch, whereas the cell structure deeper inside remains mostly intact.

The μCT images in Fig. 13 illustrate the scratch grooves generated in the heartwood sample 64. The images show the horizontal cross sections taken 0.1–0.2 mm below the sample surface representing the scratches made in the radial, tangential, and longitudinal directions with normal loads of 4, 10, and 20 N. Prominent crack formations appear on the sides of the scratch grooves perpendicular to the scratches when the scratching direction was radial and tangential, whereas in the longitudinal direction similar crack formations were not observed. The performance was influenced by the structural orientation of wood, since scratching in radial (tangential to the growth rings) and tangential directions (along the growth rings) goes perpendicular to the grain structure of the wood, whereas the longitudinal direction (along the length of the wood) goes parallel to the grain structure.

The figure also shows that the scratch-induced cracks appear strongest when the indenter penetrates deeper, indicated by a wider scratch groove. These areas correspond to the softer areas of wood that typically represent the early wood. On the harder regions representing the late wood, the penetration of the indenter is lower, which corresponds to findings of a previous study [4].

The different failure mechanisms are revealed in the high-resolution μCT image in Fig. 13b showing the cross section of the scratch groove in the longitudinal scratch. The densification of the wood cells under the scratch load can be clearly seen, including complete collapse of some cells. The cracks due to shear action caused by the movement of the scratch indenter also propagate to generate large fractures in the wood cell structure leading to detached wood fragments.

The differences between the heartwood and sapwood samples can be observed in Fig. 14. The heartwood sample 64 suffered severe fractures, particularly along the scratch groove length. The fractures became more pronounced as the normal load was increased, showing pull-out of fractured material. Cracking and fractures can also be observed around the scratch in the cross-sectional areas. Also, the scratch depth increased with increasing normal load. Sample 69, representing the sapwood, with higher density, had similar structural

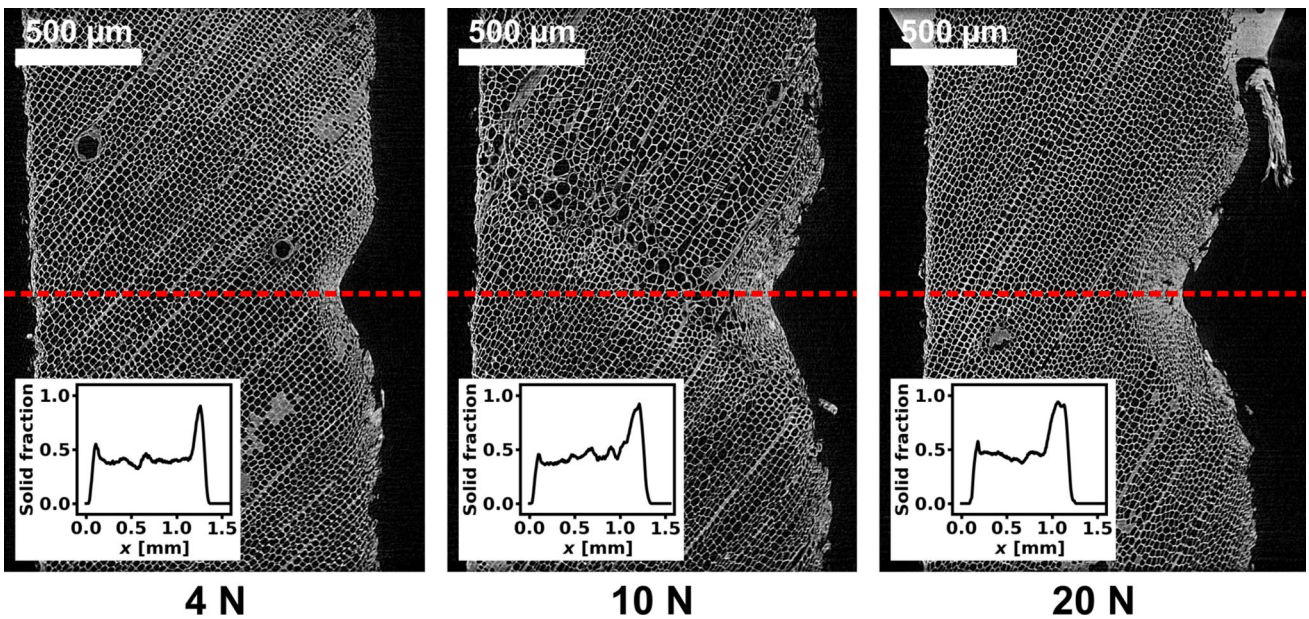

Figure 12 High-resolution μCT images of wood sample 64 after scratch testing in the L direction under three different normal loads (4, 10, and 20 N). The accompanying graphs show the solid fraction profiles across the wood sample (indicated by dashed lines), indicating a sharp-edged densification layer near the surface of the scratch.

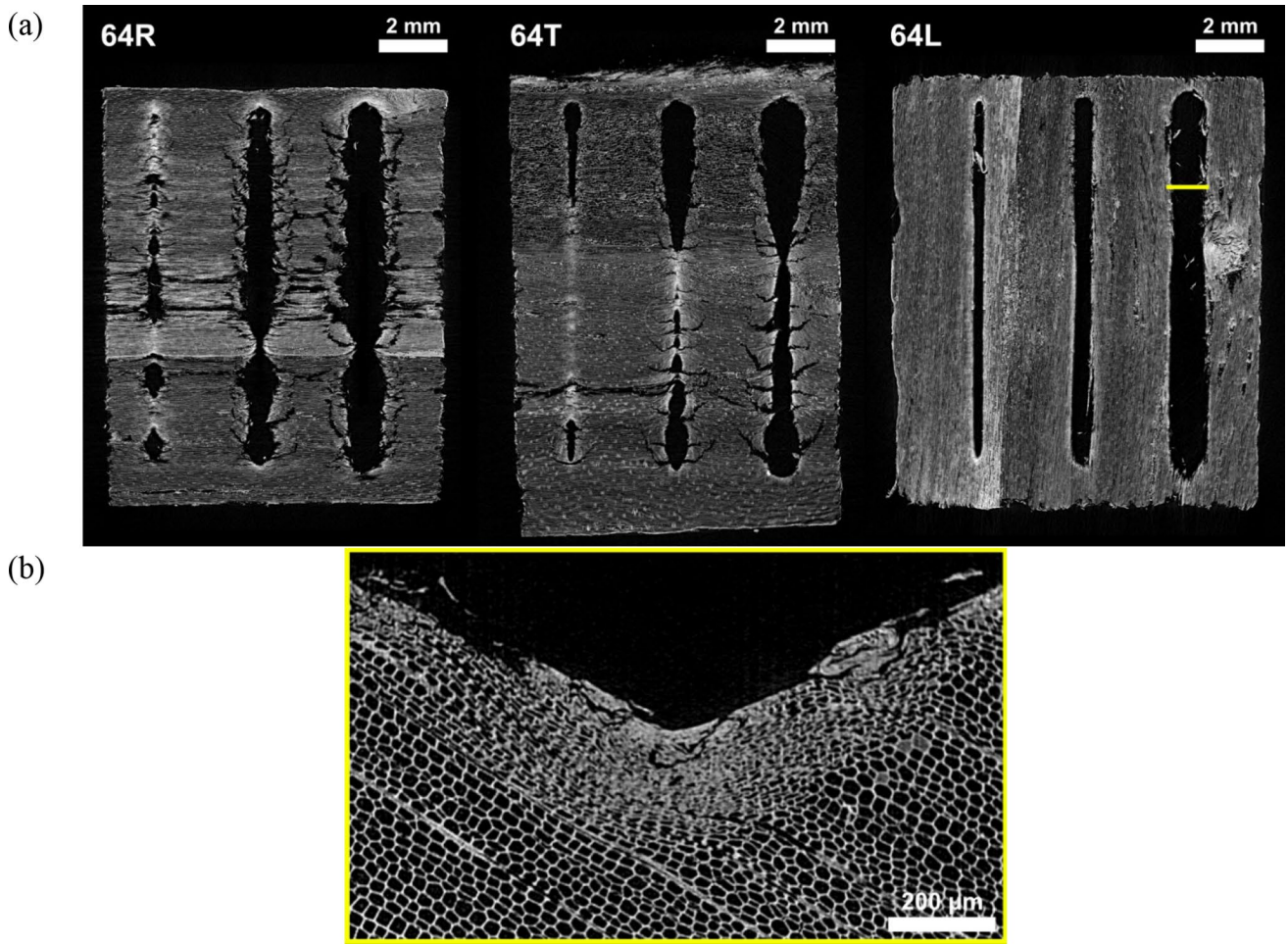

Figure 13 The μCT images of heartwood sample 64 after scratch tests showing **a** the horizontal cross sections with medium resolution taken 0.1–0.2 mm below the sample surface, corresponding to scratches made in the radial (R), tangential (T), and longitudinal (L) directions with normal loads of 4, 10, and 20 N represented from left to right in each image. **b** The cross section of the longitudinal scratch groove corresponding to the position indicated by a solid line in (**a**).

fractures along the scratch groove, yet the fractures were most visible only with the highest load, and they were not as severe as those observed in sample 64, representing heartwood. The cross-sectional image shows that the depth of the scratch groove was much smaller compared to sample 64, and with less cracking of the wood structure. These results suggest that the density of the wood structure has a strong influence on the scratch resistance of the wood and the failure mechanisms of the wood under scratch loading.

Finite element modelling of deformation of wood structure under scratch load

A series of 2D finite element simulations was conducted to model the scratching process under three different loads. Figure 15a presents the results for one of the loading cases of 62 N (corresponding to 20 N in 3D; see Sect. "Finite element modelling of wood structure"), showing the von Mises stress field in the deformed wood structure at the moment when the load on the indenter reaches its maximum. The stress distribution was highly non-uniform, with pronounced concentrations that could potentially act as sites for damage nucleation. The residual strains after load release and relaxation are presented in Fig. 15b. Similar to the stress distribution in Fig. 15a, distinct localizations were observed, although the affected areas were smaller. Regions with plastic strains of 10% and above extended to a depth of about two times the residual penetration depth (visible as greenish and reddish areas).

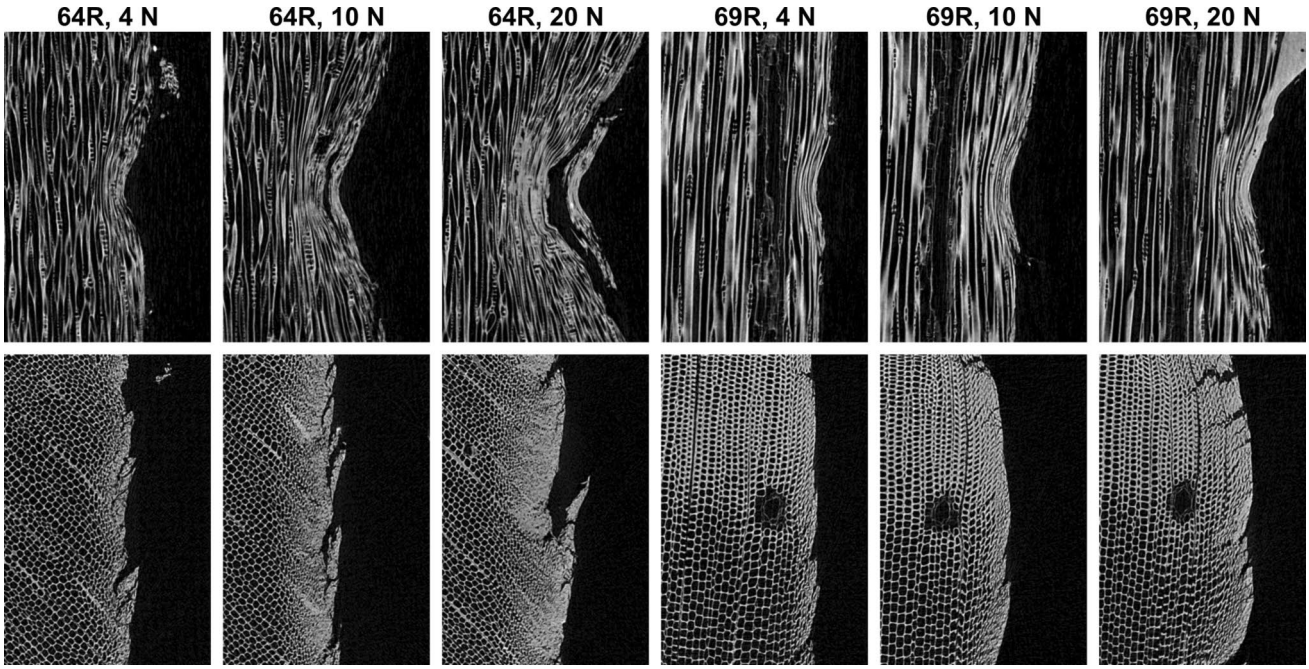

Figure 14 High-resolution μCT images of scratched heartwood sample 64 and sapwood sample 69. The scratching was performed in the R direction with normal loads of 4, 10, and 20 N. The upper row shows cross sections perpendicular to the scratch groove, and the lower row cross sections along the scratch grooves (scratching direction upwards). Each image covers a 0.90 mm × 1.35 mm area.

A comparison of the residual scratch depth values from the experiment and simulation is presented in Table 3 for all three considered loadings. In all cases, the obtained numerical results were considered acceptable, with a maximum deviation of 12% observed for the lowest load. The residual displacement fields are depicted in Fig. 16. As in Fig. 12, the results are accompanied by solid fraction plots to illustrate densification. Although the residual deformations were of similar magnitude, the material densification was less localised in the contact area and extended deeper into the material in the simulations compared with the experimental observations.

To complement the main simulations, two auxiliary problems were solved to assess the influence of material orientation on scratch resistance, as described in Sect. "Finite element modelling of wood structure". The residual scratch depth values for the radial orientation were 0.112 mm, whereas for the tangential it was 0.105 mm. These values can be compared with the depth of 0.110 mm for the arbitrary orientation in the main problem (see Table 3).

Discussion

The performance and deformation of wood under load were studied by scratch tests, X-ray microtomography, and finite element simulations. In the scratch tests carried out with a diamond indenter in three scratch directions, the inhomogeneous structure of wood caused a complex evolution of the friction force and the penetration depth during scratch testing. Particularly in the R direction, high fluctuations in friction force and penetration depth values occurred due to the indenter travelling through the annual ring structure.

Friction is the force resisting the relative movement of a component on the surface, and it can be divided into adhesive and ploughing mechanisms. Adhesive contacts between the solid surfaces cause adhesive friction to occur, and deformation of the surface causes ploughing friction ([29, 30]). Concerning the scratch tests on wood samples, the ploughing mechanism had a major effect on the friction performance. The wood structure is heterogeneous, with growth rings consisting of soft earlywood and harder latewood. Therefore, the scratching, particularly in the radial direction,

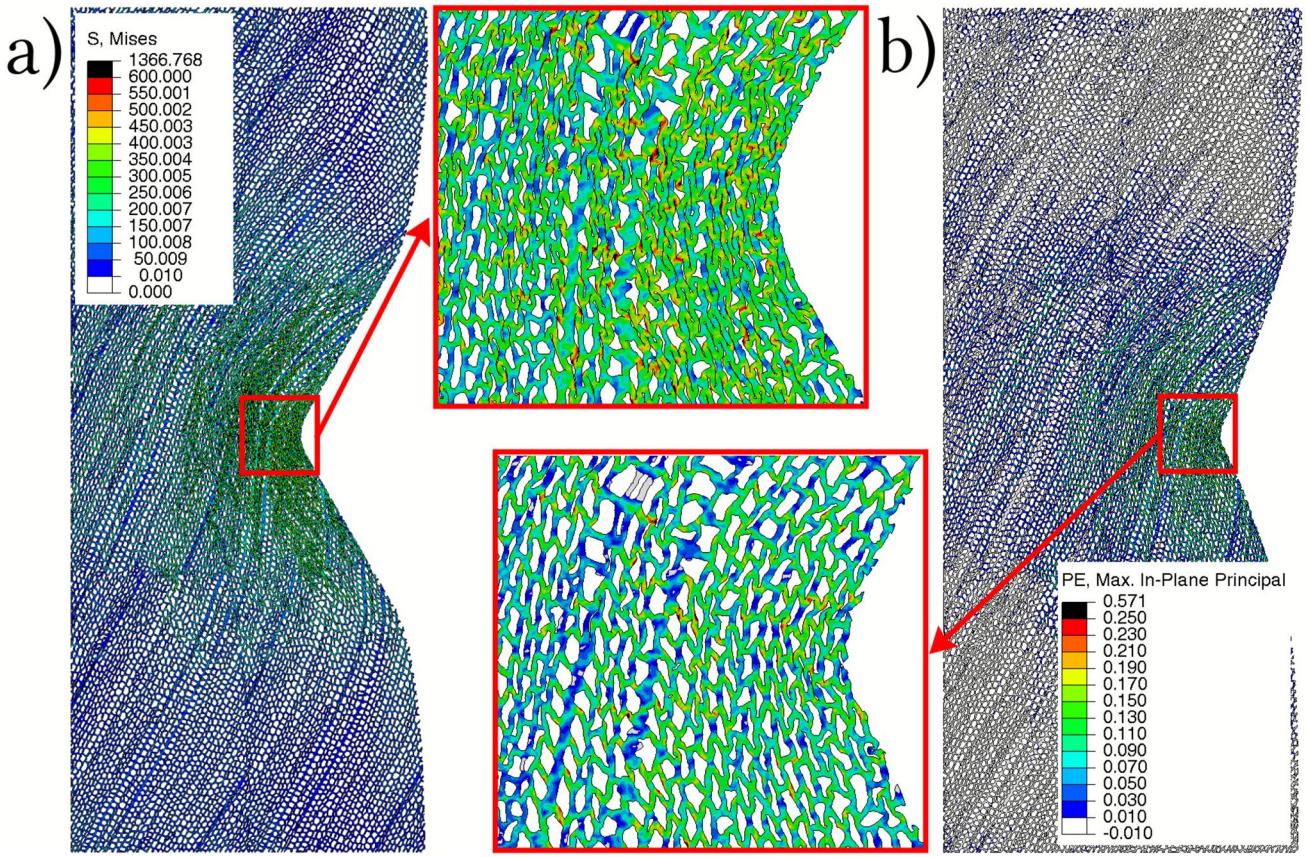

Figure 15 Results of Finite Element Modelling for the loading equivalent to 20 N. **a** von Mises stress at the moment of maximum load and deformation. **b** Maximum in-plane principal plastic strain after relaxation.

Table 3 Comparison of residual scratch depth [mm] between experimental measurements and simulation results for all considered load cases

Loading	4 N	10 N	20 N
Experiment	0.125	0.223	0.313
Simulation	0.110	0.210	0.323
Difference	−12.0%	−5.8%	3.2%

The percentage difference is calculated for the simulation with respect to the experimental values

against the growth rings, caused high variation in the friction force. The friction force was connected to the evolution of penetration depth that followed the structural features of the wood structure. The variation in friction force and penetration depth was most evident in the radial direction of the wood, whereas the tangential and longitudinal directions showed more even performance in scratch testing along the scratch groove.

The density of wood samples influenced the performance in scratch tests, showing reduced friction force with increasing density as depicted in Fig. 8. The density also influenced the penetration depth, as observed for higher density sapwood that experienced both lower penetration depth and friction force compared to heartwood, as observed in Fig. 9a. A higher shear strength value was measured for the sapwood, which suggests that higher density was also associated with higher shear strength.

The friction force and the penetration depth measured during the scratch tests increased with increasing normal load. The μCT imaging provided data on the depth of the scratch grooves generated in the wood surface. The penetration depth measured during scratch testing represented the entire deformation during scratch testing, consisting of both plastic and elastic deformation of the wood, whereas the μCT imaging of the scratched samples provided information on the residual deformation of the wood, representing the non-recoverable plastic deformation. The difference

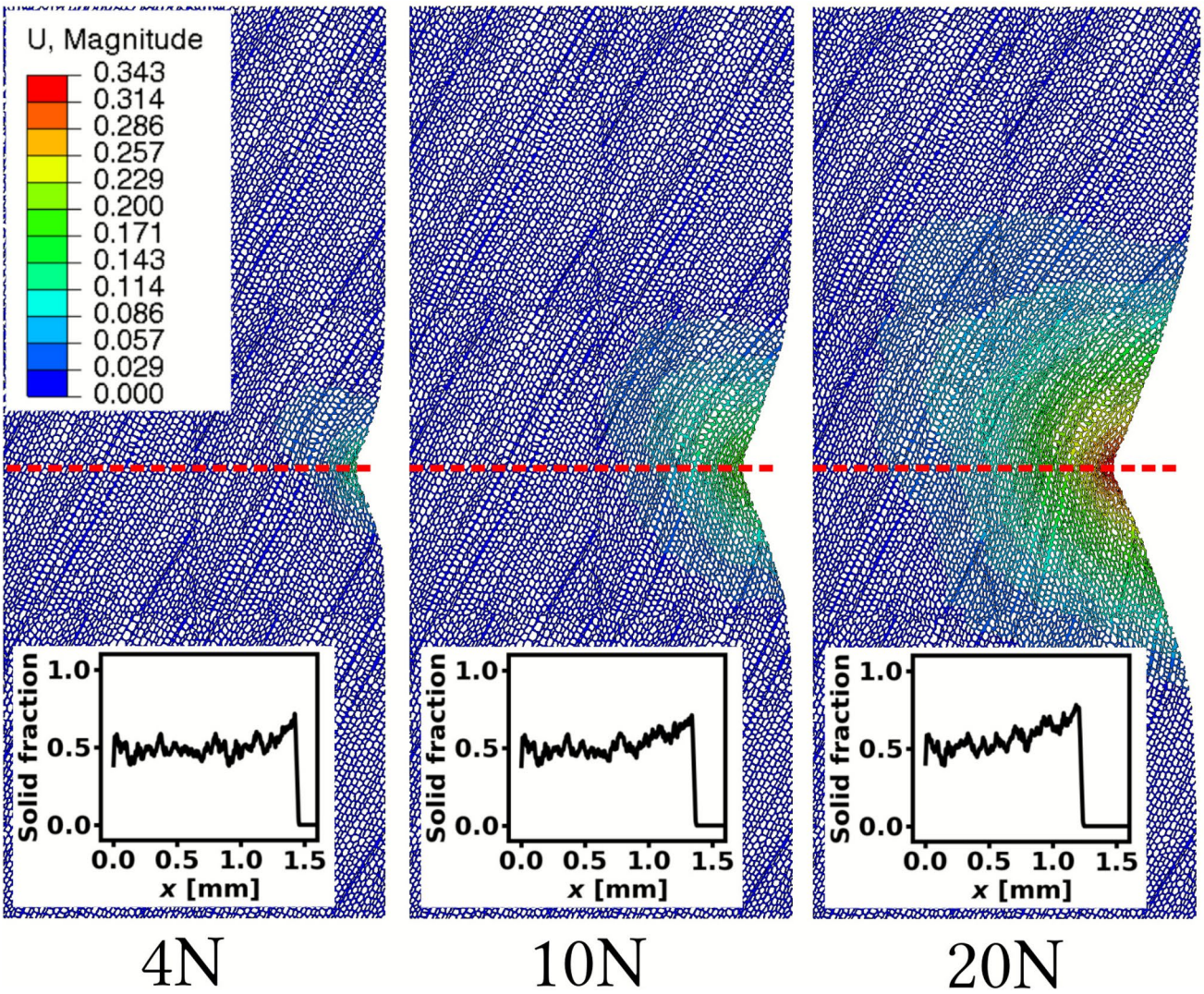

Figure 16 Finite element simulation results showing the residual deformation [mm] in the samples for all considered loadings (4, 10, and 20 N). The accompanying graphs show the solid fraction profiles across the wood sample (indicated by dashed lines). See Fig. 12 for a comparison with the experimental results obtained by μCT.

between these two represented the elastic deformation, showing the recovery of the wood structure. The results showed that the sapwood with higher density experienced mostly elastic deformation during scratch testing, as observed in Figs. 9 and 10. This suggests that the higher density of wood favours elastic deformation and higher recovery of wood after the scratch load is released. The heartwood exhibited higher plastic deformation compared to sapwood, as observed in Fig. 11, where the residual depth values are presented. The slope in the graph describing the friction force as a function of plastic deformation in Fig. 9 shows that sapwood has a higher slope compared to heartwood, which can be related to the higher scratching resistance of denser sapwood compared to heartwood. This trend is most evident for scratches generated in the radial and tangential directions of the wood samples.

The wood structure influenced the deformation performance in different scratch directions. When the scratch test was carried out in the radial or tangential direction, elastic deformation was dominant for all samples, but scratching in the longitudinal direction showed more plastic deformation. This difference in behaviour can be clearly observed in Fig. 10 which shows the ratio of elastic deformation to plastic deformation for heartwood and sapwood samples in

different directions and normal loads. Thus, higher density wood can be more tolerant to different types of scratching mechanisms or mechanical wear of wood surfaces and has therefore better scratch resistance.

The μCT imaging proved to be a good tool to determine the residual depth of the scratch grooves. Validation showed that the fitting processes in the image analysis were accurate for the scratches with well-defined cross-sectional shapes (as shown in Fig. 4). However, highly irregular scratches, resulting from the performance of the wood structure under the scratch load, could lead to some inaccuracies. The main limitation of the μCT method comes from the long imaging time, and therefore faster techniques such as, e.g. 3D profilometry could be applied if applicable for the material. Previously used methods for detecting scratch resistance of wood have been mostly based on scratching with different normal loads and visually detecting the generated scratches on the wood surfaces ([31, 32]). In this study, the combination of scratch test and μCT imaging provided a quantitative method for measuring the residual plastic deformation of the scratch groove, which provided a quantitative means of determining the scratch resistance. Sapwood with higher density had lower residual depth of the scratch grooves thus showing higher scratch resistance compared to heartwood. The sapwood had also higher shear strength, which suggests that higher density wood is related to higher shear strength and further to more elastic deformation under scratch loading.

The μCT imaging of the scratched samples revealed the densification of the wood structure under scratch load. With the increase in the normal load, the depth of the densified layer increased. With the highest applied load, even in the longitudinal direction, some fractures in the cell structure were observed, as shown in Fig. 12. When the scratches were made in the radial and tangential directions against the growth rings, the loading conditions were more severe, causing structural failures. Besides densification, the wood structure experienced cracking and fracture generation beneath and around the scratch groove as observed in Figs. 13 and 14. The μCT images revealed that deformation and fracture mechanisms in wood under scratch-type loading were highly complex and strongly direction-dependent. Fracturing was more pronounced when scratching was applied perpendicular to the grain (radial and tangential directions) compared to scratching along the grain (longitudinal direction). The orientation of fractures, both along and against the scratching direction, suggests that multiple stress components contribute to the initiation and propagation of failures. The fractures along the scratch groove were more severe for heartwood, showing large, fractured fragments detached from the surface along the scratch groove. Similar failure features can also be observed for the sapwood, but at a lower intensity, as observed in Fig. 14, suggesting that higher density wood is more resistant to crack and fracture generation. In scratch testing, the contact area under the indenter experiences compressive, tensile and shear stresses. These complex loading conditions facilitate crack initiation and growth in the cell structure leading to fractured fragments to be released from the cell structure. The μCT images show that almost all plastic deformation occurs in a layer near the (deformed) surface, agreeing well with the everyday observation of restoring scratched wood surfaces by removing a thin layer, for example, by sanding.

Concerning the finite element modelling, although the values of residual depths from modelling are similar compared to experimental values, the overall deformations are much more localised around the contact area with the indenter as can be observed when comparing the solid fraction plots in Figs. 12 and 16. Overall, plastic deformation predicted by the modelling was distributed over a relatively large volume, but the values of the strains remained in the range of 1–3%. It was also observed that during deformation the gaps between cells were not fully closed, and despite clear densification around the area of contact between the material and indenter, the structure retained its cellular character after the relaxation of elastic strains, even in the presence of significant local plastic deformations. The simulations also tended to underestimate the level of densification of the wood structure, which is evident in the μCT images.

The additional simulations conducted when the structure is oriented such that the indenter loads are in the radial and tangential wood directions, provided some evidence of the applicability of simple models for assessing the role of anisotropy in scratch resistance. It is worth mentioning that the model still represents the behaviour in the cross

section normal to the longitudinal scratching direction, as described in Sect. "Finite element modelling of wood structure", while the material is effectively "rotated" within this cross section, thereby changing the wood direction of indentation. The residual scratch depth in the tangential wood direction is about 6% lower than in the radial wood direction and about 5% lower than in the arbitrary orientation used in the experiment.

The authors would like to emphasise that the presented finite element simulation was intended as a demonstration of the applicability of the approach and represents an initial attempt. Although it produced reasonably good results in terms of residual deformation, further improvements are necessary. For example, in the 2D model, it is not possible to evaluate shear stresses and strains, since during scratching they develop in the third direction, which coincides with the movement of the scratching indenter and is not represented in the model. The modelling options include more sophisticated material models for wood cell structures incorporating nonlinear plasticity, viscoelasticity and appropriate damage initiation and propagation models, e.g. the multisurface failure criterion used by Lukacevic et al. in [33] or Hill's failure criterion discussed by Akter and Bader [34], as well as a full-scale 3D model. To complement the study, two types of 3D models could be considered: a micro-scale model, similar to the presented 2D version, to further investigate micro-effects, and a microstructure-informed homogenised macro-scale model to simulate the scratching process at full.

Compared to previous scratch test studies on wood [4, 12], the presented methodology allows for a detailed analysis of both the elastic and plastic performance of wood under scratch loads, specifically at the cellular level, by utilising μCT and numerical models. The confocal microscopy used in [4] could not capture the scratch induced crack initiations. On the contrary, in the present research the high-resolution μCT images could detect in detail the crack formations in the vicinity of the scratch grooves. By considering how the material behaves microscopically under compressive, tensile, and shear stresses that affect deformation and failure mechanisms, these findings can be applied to various disintegration processes in the construction industry. Furthermore, the precision of μCT images before and after scratching allowed the creation of a first numerical model for wood scratch testing. Additionally, developing reliable numerical models is crucial for future investigations into other micro-scale disintegration mechanisms, such as cutting wood and wood-based composites.

Conclusion and future work

In this research, scratch testing on untreated pine wood samples and investigation of scratches by utilising μCT were introduced as a new methodology to assess plastic deformations in scratched wood. These outcomes extend the understanding of the performance of wood under scratch loads.

Basic research findings are the following:

- The friction force between the scratch tip and the pine wood decreased with increasing density of the wood in the range of 400–550 kg/m^3.
- The friction force increased with increasing load and increasing penetration depth.
- Higher density of sapwood was associated with higher shear strength and higher elastic deformation under scratch loads.
- Higher density also resulted in lower penetration depth and friction force in scratch testing.
- The residual depth of scratches described the plastic deformation of the wood, thus representing the directly measurable scratch resistance of the wood. The higher density of wood favoured lower residual depth thus providing higher scratch resistance for sapwood in this case.
- The combination of scratch testing and μCT imaging can be used for detecting the wood performance under scratch loads and to verify the scratch resistance of the wood.
- μCT imaging provided accurate insights into the complex deformation and fracture mechanisms of wood under scratch-type loading, including densification, cell collapse, crack and fracture propagation beneath and around the scratch groove.

- μCT imaging combined with modelling enhanced the understanding of the performance of the wood structures under different loading conditions.

The presented methodology can be used for the evaluation of scratch resistance of different wood-based products, especially for products where the scratch resistance is relevant, also for aesthetic reasons, e.g. flooring and decking boards, cladding boards and panels. The methods can also be applied for the development of new wood-based composites, such as the transparent wood [35], for different industrial sectors, such as automotive, construction, furniture and electronics.

This study has confirmed that the friction force under scratch test loads exhibits a linear dependence on the penetration depth in terms of both the total depth (elastic and plastic deformation) and the residual depth (plastic deformation). A similar linear dependence was found in cutting tests of wood where the cutting force, and therefore the cutting resistance, is defined as a linear function of the uncut chip thickness [36]. In the 5G-Timber project [37], it was argued that a relationship between the scratch resistance and the cutting resistance in wood should exist. Even if more research is needed to establish such a relationship, the results presented in this paper could be used as a reference for future studies on cutting resistance of wood, with focus on the effects of wood directions, density and wood type, in order to optimise cutting operations with consequent energy saving in sawmills and other woodworking industries.

Finally, the same μCT technology adopted in this work was used by some of the authors in [38] to accurately measure the total water in wood and the free water in lumens and to predict the bound water in wood cell walls under moisture variations, along with the assessment of a multi-phase moisture transport model for the same pine wood investigated in the present study. Based on this, the scratch resistance of wood products under moisture effects could be accurately investigated by further developing the methodology proposed in this paper.

Acknowledgements

The work carried out in this paper received funding from the Academy of Finland project WaterInWood (Decision number 349194). It was also supported by the 5G-Timber project, HORIZON-CL4-2021-TWIN-TRANSITION-01-21 (Grant Agreement 101058505), funded by the European Union. Views and opinions expressed are, however, those of the authors only and do not necessarily reflect those of the European Union. Neither the European Union nor the granting authority can be held responsible for them. The AI-TranspWood project, HORIZON-CL4-2023-RESILIENCE-01-23 (Grant Agreement 101138191) is also acknowledged. This project is co-funded by the European Union. Views and opinions expressed are, however, those of the author(s) only and do not necessarily reflect those of the European Union or HaDEA. Neither the European Union nor the granting authority can be held responsible for them. Dr. Yu Jiang and Mr. Risto Parikka at VTT are acknowledged for the scratch testing experiments.

Funding

Open Access funding provided by Technical Research Centre of Finland.

Declarations

Conflict of interest On behalf of all authors, the corresponding author states that there is no conflict of interest.

Appendix 1

See Tables 4 and 5.

Table 4 The average and standard deviation values of friction force (Fμ) measured from three similar samples

Sample no	Density Ru kg/m³	Friction force, Ft [mN]																	
		Scratch direction R						Scratch direction T						Scratch direction T					
		4 N		10 N		20 N		4 N		10 N		20 N		4 N		10 N		20 N	
		average	stdev	average	stdev	average	stdev	average	stdev	average	stdev	average	stdev	average	stdev	average	stdev	average	stdev
44	499	1918.0	576.5	5102.6	1761.8	9720.0	3592.3	2294.9	269.6	6181.3	1205.9	11890.1	1944.7	2280.9	299.3	5379.6	649.8	10122.4	1066.0
45	529	2696.9	480.4	6612.5	1225.2	13162.6	2459.6	1931.9	296.3	5396.6	761.6	10320.0	1605.6	2245.7	291.0	6613.6	665.9	12561.3	1709.8
46	538	2122.7	449.5	5371.1	1476.1	7593.8	1202.9	2179.1	453.2	5826.6	925.2	10659.0	1901.2	2099.9	186.8	5060.8	703.8	8991.2	1066.5
47	470	2941.3	603.4	6931.7	1616.3	11791.6	2887.0	1541.7	354.8	4593.4	590.2	9333.1	1105.7	2478.8	436.8	6607.0	758.7	11475.4	1923.4
48	469	2843.8	509.3	7144.8	1414.8	13696.4	2989.1	2495.7	387.8	4921.3	1077.8	8770.2	1734.4	2249.7	291.7	5082.2	724.7	8354.6	1344.0
49	530	2635.7	491.1	5292.7	1233.9	11559.7	2068.4	2315.8	711.6	5708.8	1420.3	11351.8	2748.0	2144.8	354.5	4001.4	533.7	9179.7	1277.5
50	484	1981.5	492.3	4365.9	758.8	9751.6	1514.6	2203.3	709.6	6129.3	1736.8	11652.5	3347.7	2326.4	228.4	5988.3	880.9	11897.5	1840.4
51	493	2094.1	822.4	6080.2	2003.6	13572.7	3480.9	2513.3	408.3	6175.1	1092.8	11002.0	1763.3	2314.0	285.2	6362.3	1059.3	11255.9	2152.1
52	445	2736.8	673.0	6692.6	1668.5	10577.7	2746.2	3012.6	615.0	6277.3	1137.5	9465.3	1384.3	2855.0	275.1	4620.6	652.6	8122.1	826.7
53	454	2478.1	518.2	6771.9	1074.6	13796.8	2265.2	2641.9	468.1	6949.6	906.3	13183.2	2297.1	3246.4	452.8	6491.9	841.7	12507.6	1219.8
54	469	2130.7	656.6	6304.4	1773.6	13106.3	3599.0	2588.9	617.1	5722.2	773.5	9348.7	1644.4	3572.0	356.7	5969.5	538.8	7338.7	555.7
55	462	2179.3	786.9	5744.4	1915.0	11069.6	3476.3	2589.3	406.4	5912.9	889.2	8519.9	1613.1	2343.5	287.7	5753.5	641.3	8915.6	1024.6
57	516	2306.9	984.2	6048.6	2349.7	11142.6	3584.5	2478.4	526.3	5295.0	808.0	11425.9	1805.3	2057.3	209.3	4633.6	354.4	11321.1	1303.9
58	399	3096.2	567.6	7283.4	1250.4	12191.1	2126.6	2627.6	693.9	6743.5	1236.9	12453.8	1815.5	2400.0	170.8	6000.1	632.4	7389.1	620.1
59	422	2953.8	929.8	6540.8	1624.5	12161.3	3225.8	2475.1	620.1	6867.7	1286.1	11338.9	2336.9	2663.4	231.2	4801.1	311.0	11370.0	1142.9
60	484	2684.0	753.5	7089.9	1856.3	12545.4	3221.6	2496.5	420.0	5851.1	1054.6	11824.1	2070.0	2872.4	368.9	6718.9	662.7	12181.6	1073.0
61	501	2040.3	626.9	3453.4	377.3	8535.8	2145.6	2553.2	550.8	3603.1	121.3	11414.0	1213.1	2395.9	266.8	3599.9	174.9	8513.2	907.9
62	506	2040.1	805.2	5390.5	1881.7	10641.8	3648.9	2209.3	537.2	6662.1	1058.6	13023.9	1913.4	2041.3	186.2	4501.6	526.3	8496.9	964.0
63	548	2202.2	966.9	6226.3	2419.6	13512.5	4528.3	2356.2	356.4	7233.9	1031.2	13282.7	2142.3	2142.7	213.2	5260.5	552.9	10315.9	1069.3
64	420	3133.3	466.0	8721.5	1365.1	14977.9	2953.3	2840.1	621.7	7595.3	1743.2	14323.5	2807.2	2899.6	270.2	5576.9	955.2	11330.4	1394.6
65	419	2791.8	622.9	6789.9	1391.5	11471.5	2163.7	2836.4	402.1	7707.4	877.5	11725.9	1113.6	2603.7	279.5	5774.6	877.4	9842.2	1022.0
66	484	2829.8	637.1	7235.2	1826.2	11786.4	2742.0	2287.4	432.2	5712.4	785.9	7536.5	851.6	3323.2	366.4	5728.6	1150.3	10290.9	935.0
67	496	2286.2	490.1	5689.4	1148.9	9782.5	2383.6	2371.2	303.1	6423.7	794.1	11705.2	1272.6	1866.0	152.4	4836.5	467.9	7894.3	613.3
68	519	2299.7	448.0	7232.6	1720.2	14982.1	4685.2	2203.6	179.0	6699.7	573.0	13960.1	1281.7	2318.6	249.9	5346.4	524.6	9315.7	917.1
69	556	1970.8	516.3	3525.7	616.5	11040.4	3225.4	2078.2	306.1	3739.8	220.6	8378.4	734.0	2216.3	292.0	3591.3	106.0	7536.6	969.3

Table 5 The average and standard deviation values of penetration depth (Pd) measured from three similar samples

Sample no	Density Ru kg/m³	Penetration depth, Pd [μm]																	
		Scratch direction R						Scratch direction T						Scratch direction T					
		4 N		10 N		20 N		4 N		10 N		20 N		4 N		10 N		20 N	
		average	stdev	average	stdev	average	stdev	average	stdev	average	stdev	average	stdev	average	stdev	average	stdev	average	stdev
44	499	188.8	72.4	290.7	78.2	391.6	69.5	189.4	66.3	330.9	94.4	683.1	109.3	336.2	66.3	282.5	37.0	483.6	61.7
45	529	230.8	62.4	420.5	53.2	618.3	88.9	151.1	71.5	263.8	91.4	411.4	109.4	166.9	45.1	354.4	65.4	709.3	91.7
46	538	288.1	35.6	316.0	94.8	358.3	58.9	173.6	62.0	295.5	109.5	455.4	104.3	313.1	20.6	261.7	65.9	567.6	96.0
47	470	208.0	75.3	327.8	85.0	443.2	70.3	86.1	14.6	162.1	16.7	298.2	28.5	334.9	44.0	481.4	45.2	460.1	94.3
48	469	327.6	58.8	377.7	76.4	580.3	101.8	259.9	105.8	334.7	87.4	407.2	55.8	306.6	45.2	495.9	53.6	641.7	59.1
49	530	280.9	42.8	362.0	60.2	476.9	71.8	196.5	63.7	323.9	105.9	435.6	106.2	320.1	74.7	425.9	46.8	566.2	49.0
50	484	280.9	42.8	362.0	60.2	476.9	71.8	196.5	63.7	323.9	105.9	435.6	106.2	320.1	74.7	425.9	46.8	566.2	49.0
51	493	173.6	74.2	314.1	97.2	678.0	98.3	275.0	56.8	416.4	90.9	526.7	101.1	346.8	46.2	443.8	58.0	490.9	61.5
52	445	201.0	71.7	370.8	109.5	452.8	68.7	250.7	41.1	392.1	44.2	462.4	35.1	295.4	79.3	402.4	47.7	497.1	54.4
53	454	246.9	74.1	371.7	118.5	564.3	124.7	194.8	63.6	321.1	110.6	472.0	125.7	281.8	28.3	477.2	52.7	327.8	54.3
54	469	202.1	72.8	329.0	111.1	482.0	104.4	326.3	80.0	550.2	77.1	492.7	110.4	266.5	63.4	274.0	31.3	519.5	19.3
55	462	202.7	87.9	382.3	107.3	432.6	72.4	310.1	56.8	408.5	74.0	440.4	62.7	125.9	23.1	286.7	31.4	464.3	34.8
57	516	187.6	64.4	321.9	96.0	485.5	83.8	287.5	105.1	366.0	99.3	524.1	121.9	178.8	44.2	337.5	22.6	339.5	13.3
58	399	236.3	61.4	411.1	85.4	557.1	78.8	229.7	114.1	371.3	166.5	737.2	154.9	97.5	10.4	688.3	43.4	582.9	39.5
59	422	230.8	86.3	317.2	94.2	450.7	94.0	424.4	96.8	721.6	85.8	806.3	119.2	259.9	10.5	429.4	13.0	447.4	14.3
60	484	220.7	63.4	381.4	102.8	782.2	121.4	309.8	77.1	354.8	91.9	642.8	131.2	128.4	17.7	304.1	32.4	453.9	32.4
61	501	229.2	72.7	332.7	64.3	455.3	68.4	215.1	82.9	348.2	118.3	492.4	140.7	114.4	32.3	210.5	22.8	320.6	10.7
62	506	193.2	69.9	312.6	97.4	453.9	81.1	313.7	47.6	471.5	110.4	846.5	104.5	310.3	20.0	356.8	17.1	451.9	12.4
63	548	172.1	61.8	257.9	67.5	667.6	73.5	199.2	99.9	421.1	127.0	720.5	148.8	144.2	18.8	325.6	92.5	369.3	28.1
64	420	180.5	39.4	343.3	58.8	778.4	54.4	317.2	43.3	489.9	58.7	760.5	47.2	176.3	45.0	297.4	29.7	434.9	26.7
65	419	249.4	34.1	422.8	72.1	559.2	82.1	176.1	41.8	358.3	66.6	479.2	60.7	140.7	19.3	349.0	17.7	465.3	23.5
66	484	218.7	45.7	363.8	99.7	484.2	100.1	252.5	63.3	414.2	85.5	549.5	123.5	241.4	25.9	407.1	61.9	396.0	39.4
67	496	217.3	64.7	338.8	74.8	435.0	68.3	174.2	38.4	321.4	51.4	506.4	69.9	217.9	9.8	442.2	42.6	498.9	33.9
68	519	231.6	57.0	344.4	108.3	498.3	104.9	107.0	5.8	196.4	11.0	313.4	15.7	287.4	26.9	421.1	14.0	486.7	17.4
69	556	187.8	59.3	270.1	92.5	397.2	96.1	290.2	59.8	392.8	32.2	553.4	55.9	80.7	13.4	336.0	23.5	472.1	10.8

Appendix 2

See Figs. 17, 18 and 19.

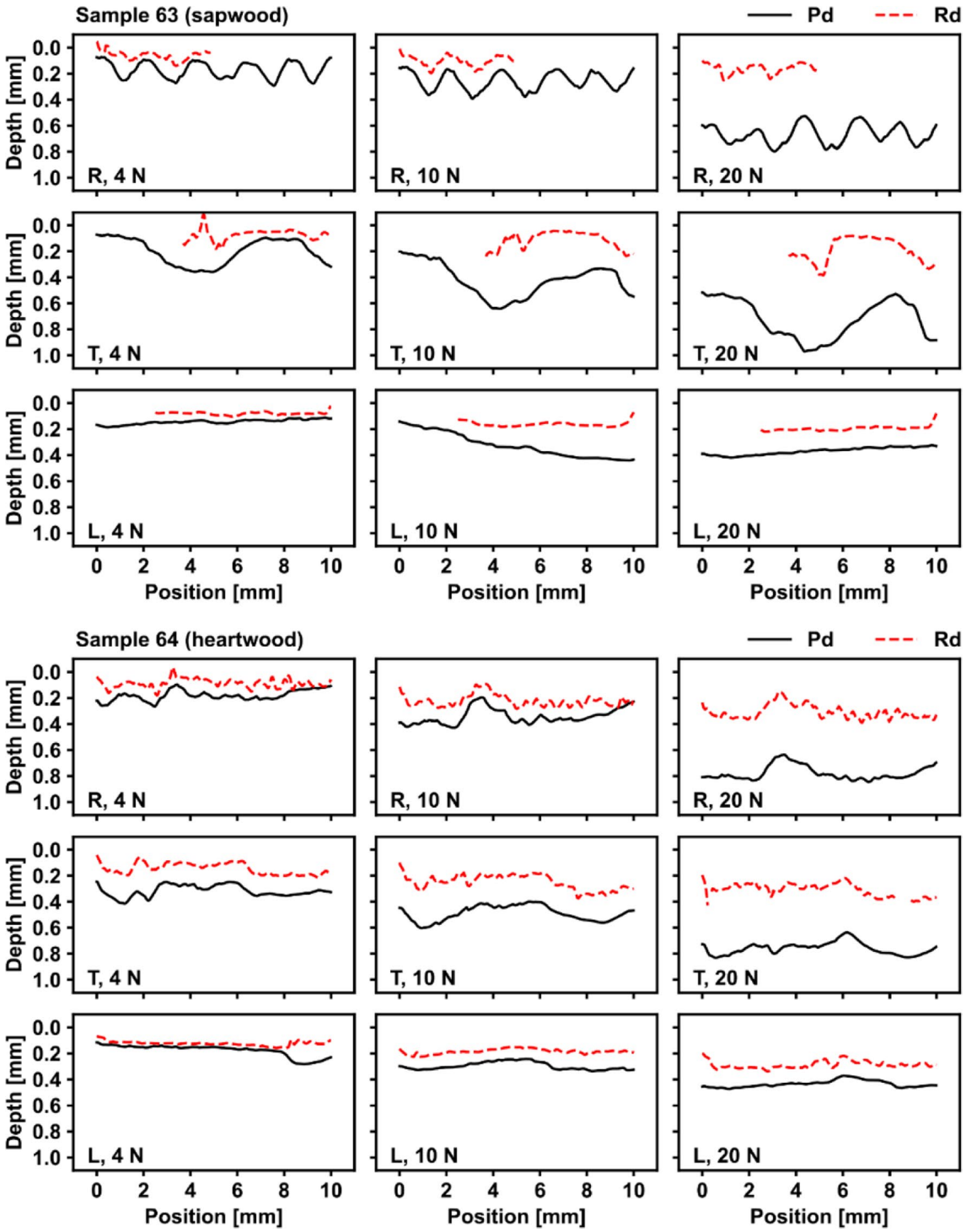

Figure 17 Penetration depth and residual depth profiles of all scratches on samples 63 and 64. The penetration depth (Pd) was obtained from the scratch test device, and the residual depth (Rd) was measured from the medium resolution μCT post-scratch images. The scratching direction (R = radial, T = tangential, and L = longitudinal) and the normal load (4, 10, and 20 N) are indicated in each subfigure. Subsamples from sample 63 were inadvertently cut for high-resolution μCT scans before medium-resolution μCT scans, and therefore, the residual depths of the scratches could not be measured along the entire length of the scratches.

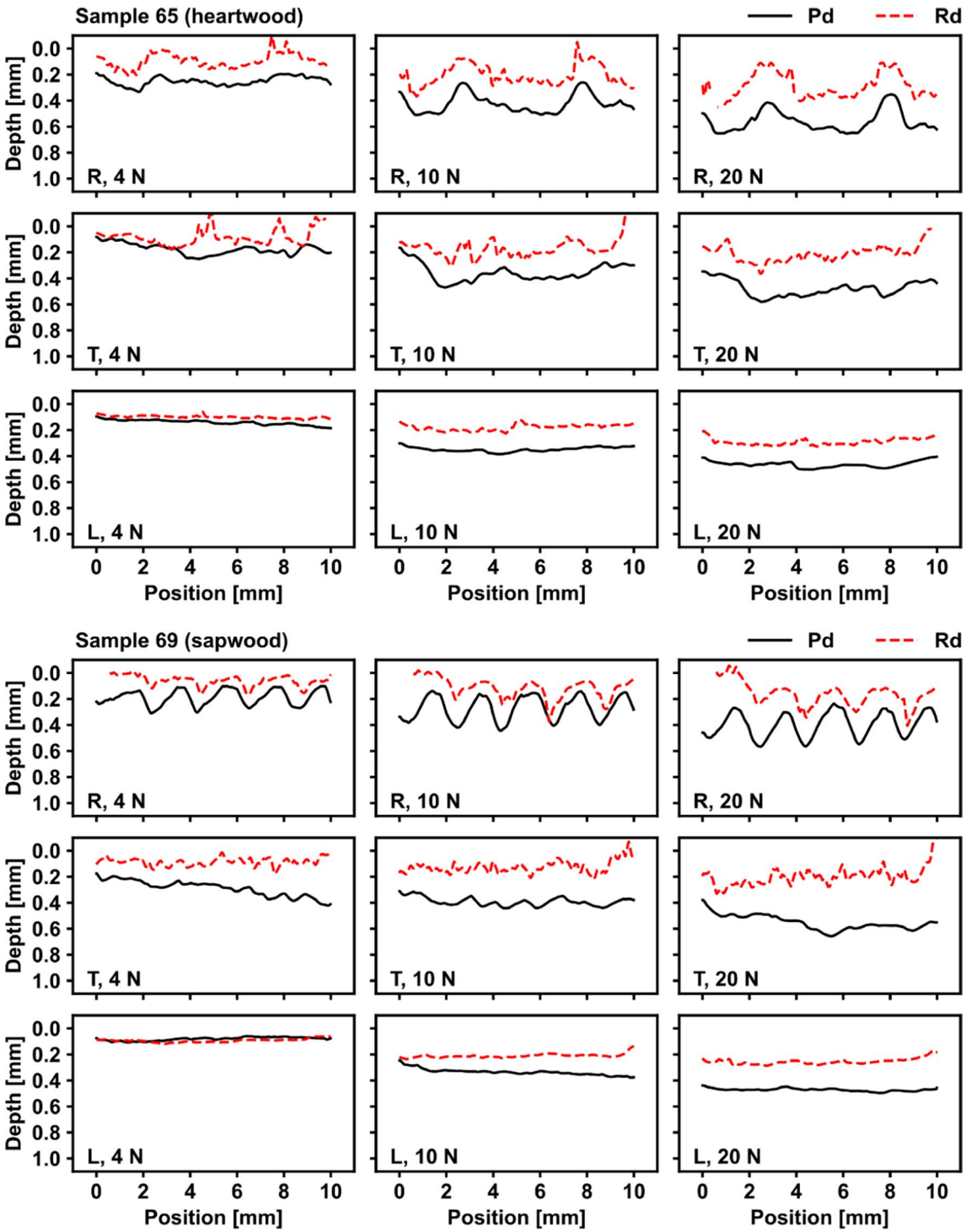

Figure 18 Penetration depth and residual depth profiles of all scratches on samples 65 and 69. The penetration depth (Pd) was obtained from the scratch test device, and the residual depth (Rd) was measured from the medium resolution μCT post-scratch images. The scratching direction (R = radial, T = tangential, and L = longitudinal) and the normal load (4, 10, and 20 N) are indicated in each subfigure.

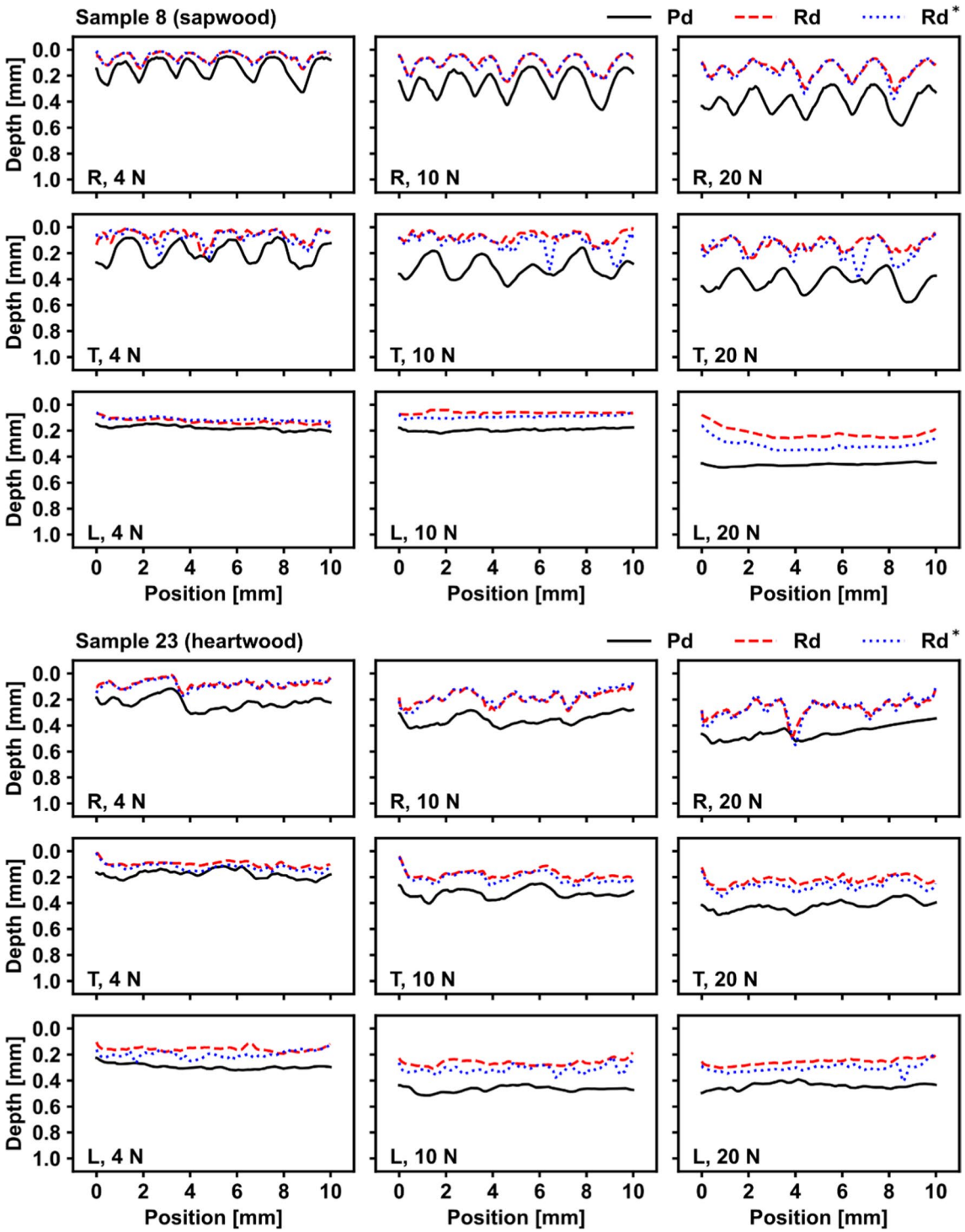

Figure 19 Penetration and residual depth profiles of all scratches on samples 8 and 23. The penetration depth (Pd) was obtained from the scratch test device, and the residual depth (Rd) was measured from the medium resolution μCT post-scratch images. For these samples, another method was also used to determine the residual depth (Rd*) by utilising the μCT images taken both before and after the scratching. The scratching direction (R = radial, T = tangential, and L = longitudinal) and the normal load (4, 10, and 20 N) are indicated in each subfigure.

Appendix 3

See Table 6.

Table 6 The values of the residual depths (Rd) and the widths of the scratch grooves generated in the wood samples in the scratch tests, measured with μCT

Sample no	Scratch direction	Fn [N]	Rd [mm]	Sigma [mm]	Width [mm]	Area [mm^2]
63	R	4	0.037	0.272	1.279	0.0253
		10	0.062	0.319	1.504	0.0499
		20	0.102	0.358	1.688	0.0914
	T	4	0.047	0.232	1.091	0.0271
		10	0.084	0.220	1.038	0.0466
		20	0.105	0.359	1.689	0.0942
	L	4	0.081	0.098	0.463	0.0200
		10	0.165	0.235	1.109	0.0976
		20	0.199	0.222	1.048	0.1107
64	R	4	0.088	0.183	0.862	0.0403
		10	0.223	0.290	1.367	0.1623
		20	0.310	0.358	1.687	0.2785
	T	4	0.147	0.228	1.074	0.0841
		10	0.252	0.320	1.508	0.2025
		20	0.316	0.398	1.874	0.3151
	L	4	0.124	0.150	0.705	0.0467
		10	0.185	0.193	0.911	0.0897
		20	0.289	0.300	1.414	0.2178
65	R	4	0.093	0.263	1.240	0.0613
		10	0.203	0.367	1.729	0.1866
		20	0.289	0.441	2.077	0.3200
	T	4	0.087	0.252	1.187	0.0550
		10	0.173	0.354	1.668	0.1539
		20	0.215	0.402	1.892	0.2162
	L	4	0.100	0.230	1.083	0.0577
		10	0.180	0.186	0.877	0.0838
		20	0.291	0.326	1.537	0.2380
69	R	4	0.068	0.199	0.937	0.0340
		10	0.131	0.245	1.153	0.0803
		20	0.186	0.329	1.551	0.1539
	T	4	0.087	0.200	0.943	0.0436
		10	0.126	0.284	1.338	0.0899
		20	0.202	0.363	1.708	0.1837
	L	4	0.093	0.266	1.253	0.0622
		10	0.209	0.201	0.945	0.1052
		20	0.253	0.242	1.141	0.1534
8	R	4	0.056	0.249	1.171	0.0347
		10	0.105	0.414	1.952	0.1091
		20	0.154	0.324	1.524	0.1247
	T	4	0.064	0.434	2.045	0.0696
		10	0.074	0.719	3.386	0.1340
		20	0.136	0.377	1.776	0.1281
	L	4	0.129	0.156	0.736	0.0504
		10	0.062	0.635	2.993	0.0981
		20	0.224	0.296	1.393	0.1660
23	R	4	0.079	0.174	0.820	0.0344
		10	0.188	0.278	1.309	0.1308
		20	0.267	0.362	1.704	0.2426
	T	4	0.101	0.176	0.828	0.0444
		10	0.182	0.242	1.138	0.1101
		20	0.224	0.276	1.300	0.1553
	L	4	0.166	0.233	1.099	0.0969
		10	0.200	0.205	0.966	0.1025
		20	0.317	0.353	1.662	0.2800

References

[1] Song S, Chen C, Zhu S, Zhu M, Dai J, Ray U et al (2018) Processing bulk natural wood into a high-performance structural material. Nature 554:224–228

[2] Kollmann FFP, Côte WA Jr (1968) Principles of wood science and technology. Springer-Verlag, Heidelberg

[3] Brandstätter F, Autengruber M, Lukacevic M et al (2023) Prediction of moisture-induced cracks in wooden cross sections using finite element simulations. Wood Sci Technol 57:671–701

[4] Fortino S, Metsäjoki J, Ronkainen H, Bjurhager I, Heinemann S, Salminen LI (2020) Scratch resistance of PEG-impregnated green wood: a method for evaluation of swollen wood properties. Wood Sci Technol 54:715–735

[5] Burnett PJ, Rickerby DS (1987) The relationship between hardness and scratch aadhesion. Thin Solid Films 154:403–416

[6] Ronkainen H, Holmberg K, Fancey K, Matthews A, Matthes B, Broszeit E (1990) Comparative tribological and adhesion studies of some titanium-based ceramic coatings. Surf Coat Technol 43/44:888–897

[7] Meneve J, Ronkainen H, Andersson P, Verkammen K, Camino D, Teer DG, von Stabut J, Gee MG, Jennet NM, Banks J, Bellaton B, Matthaei-Schultz E, Vetters H (2001) Scratch adhesion testing of coated surfaces-challenges and new directions. In: Mittal K.L. (ed) Adhesion Measurement of Films and Coatings, 2: 79–106

[8] Holmberg K, Laukkanen A, Ronkainen H, Wallin K, Varjus S (2003) A model for stresses, crack generation and fracture

toughness calculation in scratched TiN-coated steel surfaces. Wear 254:283–291

[9] Beamont M, Farris TN, Sun CT (1997) Scratch testing of advanced composite surfaces. Compos Part A Appl Sci Manuf 28A:683–686

[10] Banecki J (2011) Comparative studies of furniture lacquer coatings' resistance to linear scratching acc. to the method described in TS 15186:2005. Drewno. Pr. Nauk. Donies. Komunik. 54:61–80

[11] Hermann A, Giljean S, Pac M-J, Marsiquet C, Beaufils-Marquet M, Burr D, Landry V (2021) Understanding indentation, scratch and wear behavior of UV-cured wood finishing products. Prog Org Coat 161:106504

[12] Golovin YuI, Samodurov AA, Tyurin AI, Yunak MA, Vasyukova IA (2022) Profiling mechanical properties of wood via scratch tests and nanoindentation for use in dendrochronology. ISSN 1062-8738, Bull. Russ. Acad. Sci. Phys.: Physics 86: 1219–1223. © Allerton Press, Inc.

[13] Wittmann B, Gauthier C, Burr A, Agassant J-F, Favier D et al (2020) Study of scratch resistance of a hard-on-soft polymer bilayer: combination of in situ vision. X-ray tomogr Numer Simul Wear 452–453:203271

[14] Heldin M, Isaksson P, Wiklund U (2016) Initiation of wood defibration in groundwood pulping, single asperity indentation and scratching. Nord Pulp Pap Res J 31:401–406

[15] Florisson S, Gamstedt EK (2023) An overview of lab-based micro computed tomography aided finite element modelling of wood and its current bottlenecks. Holzforschung 77:793–815

[16] Florisson S, Hansson L, Couceiro J, Sandberg D (2022) Macroscopic X-ray computed tomography aided numerical modelling of moisture flow in sawn timber. Eur J Wood Wood Prod 80:1351–1365

[17] Wiese S, Dinkler D (2021) Microstructure-related modeling of timber constructions. PAMM 20:e202000278

[18] Huber JAJ, Broman O, Ekevad M, Oja J, Hansson L (2022) A method for generating finite element models of wood boards from X-ray computed tomography scans. Comput Struct 260:106702

[19] De Magistris F, Salmén L (2008) Finite element modelling of wood cell deformation transverse to the fibre axis. Nord Pulp Pap Res J 23:240–246

[20] Fortino S, Hradil P, Salminen LI, De Magistris F (2015) A 3D micromechanical study of deformation curves and cell wall stresses in wood under transverse loading. J Mater Sci 50:482–492

[21] Phan N-T, Auslender F, Gril J, Pitti RM (2024) Effects of cellulose fibril cross-linking on the mechanical behavior of wood at different scales. Wood Sci Technol 58:1555–1583

[22] Qing H, Mishnaevsky L (2010) 3D multiscale micromechanical model of wood: from annual rings to microfibrils. Int J Solids Struct 47:1253–1267

[23] Belt T, Venäläinen M, Harju A (2021) Non-destructive measurement of Scots pine heartwood stilbene content and decay resistance by means of UV-excited fluorescence spectroscopy. Ind Crops Prod 164:113395

[24] Miettinen A (2023) pi2 [Software]. GitHub. https://github.com/arttumiettinen/pi2

[25] NIST (US National Institute of Standards and Technology). (2024) OOF2 (Version 2.3.3) [Software]. US National Institute of Standards and Technology. https://www.ctcms.nist.gov/oof/oof2/

[26] Dassault Systèmes (2023). Abaqus (Version 2023) [Software]. Dassault Systèmes. https://www.3ds.com/products-services/simulia/products/abaqus/

[27] Karakoç A, Sjölund J, Reza M, Freund J, Hernandez-Estrada A, Paltakari J (2016) Modeling of wood-like cellular materials with a geometrical data extraction algorithm. Mech Mater 93:209–219

[28] Grekin M, Surini T (2008) Shear strength and perpendicular-to-grain tensile strength of defect-free Scots pine wood from mature stands in Finland and Sweden. Wood Sci Technol 42:75–91

[29] Bhushan B, Nosonovsky M (2004) Comprehensive model for scale effects in friction due to adhesion and two- and three-body deformation (plowing). Acta Mater 52:2461–2474

[30] Lafaye S (2008) True solution of the ploughing friction coefficient with elastic recovery in the case of a conical tip with a blunted spherical extremity. Wear 264:550–554

[31] ISO (2023). ISO 1518-1:2023: Paints and varnishes — Determination of scratch resistance — Part 1: Constant-loading method. International Organization for Standardization, Geneva.

[32] Keskin H, Atar M, Korkut S (2010) Scratch resistance of cellulosic, synthetic, polyurethane, waterborne, and acid-hardening varnishes used on woods. Ind Crops Prod 31:219–224

[33] Lukacevic M, Lederer W, Füssl J (2017) A microstructure-based multisurface failure criterion for the description of brittle and ductile failure mechanisms of clear-wood. Eng Fract Mech 176:83–99

[34] Akter ST, Bader TK (2020) Experimental assessment of failure criteria for the interaction of normal stress perpendicular to the grain with rolling shear stress in Norway spruce clear wood. Eur J Wood Wood Prod 78:1105–1123

[35] Kivikytö-Reponen P, Fortino S, Marttila V, Khakalo A, Kolari K, Puisto A, Nuvoli D, Mariani A (2024) An AI-driven multiscale methodology to develop transparent

wood as sustainable functional material by using the SSbD concept. Comput Struct Biotechnol J 25:205–210

[36] Orlowski KA, Ochrymiuk T, Sandak J, Sandak A (2017) Estimation of fracture toughness and shear yield stress of orthotropic materials in cutting with rotating tools. Eng Fract Mech 178:433–444

[37] https://www.5g-timber.eu/

[38] Dsouza R, Harjupatana T, Miettinen A, Brandstätter F, Harju A, Venäläinen M, Möttönen V, Borrega M, Paajanen A, Fussl J, Fortino S (2025) Multi-phase model for moisture transport in wood supported by X-ray computed tomography data. Wood Sci Technol 59:3